Bioactive Materials 42 (2024) 178–193

Contents lists available at ScienceDirect

Bioactive Materials

journal homepage: www.keaipublishing.com/en/journals/bioactive-materials

An immunotherapeutic hydrogel booster inhibits tumor recurrence and promotes wound healing for postoperative management of melanoma

Yuanyuan Yang [a,1], Bo Zhang [b,1], Yangtao Xu [a,c,1], Wenxiang Zhu [a,c], Zinian Zhu [a], Xibo Zhang [a], Wenze Wu [b,**], Jierong Chen [d,***], Zhiqiang Yu [a,*]

[a] Department of Laboratory Medicine, Dongguan Institute of Clinical Cancer Research, Dongguan Key Laboratory of Precision Diagnosis and Treatment for Tumors, The Tenth Affiliated Hospital of Southern Medical University (Dongguan People's Hospital), Dongguan, 523058, China
[b] Jingzhou Central Hospital, Jingzhou Hospital Affiliated to Yangtze University, Jingzhou, 434020, China
[c] Institute of Biomedical Health Technology and Engineering, Shenzhen Bay Laboratory, Shenzhen, 518132, China
[d] Laboratory Medicine, Guangdong Provincial People's Hospital, Guangdong Academy of Medical Sciences, Guangzhou, 510080, China

ARTICLE INFO

Keywords:
Glutamine metabolism
Immunotherapy
Hydrogel
Melanoma
Wound healing

ABSTRACT

Low tumor immunogenicity, immunosuppressive tumor microenvironment, and bacterial infections have emerged as significant challenges in postsurgical immunotherapy and skin regeneration for preventing melanoma recurrence. Herein, an immunotherapeutic hydrogel booster (GelMA-CJCNPs) was developed to prevent postoperative tumor recurrence and promote wound healing by incorporating ternary carrier-free nanoparticles (CJCNPs) containing chlorine e6 (Ce6), a BRD4 inhibitor (JQ1), and a glutaminase inhibitor (C968) into methacrylic anhydride-modified gelatin (GelMA) dressings. GelMA-CJCNPs reduced glutathione production by inhibiting glutamine metabolism, thereby preventing the destruction of reactive oxygen species generated by photodynamic therapy, which could amplify oxidative stress to induce severe cell death and enhance immunogenic cell death. In addition, GelMA-CJCNPs reduced M2-type tumor-associated macrophage polarization by blocking glutamine metabolism to reverse the immunosuppressive tumor microenvironment, recruiting more tumor-infiltrating T lymphocytes. GelMA-CJCNPs also downregulated IFN-γ-induced expression of programmed cell death ligand 1 to mitigate acquired immune resistance. Benefiting from the amplified systemic antitumor immunity, GelMA-CJCNPs markedly inhibited the growth of both primary and distant tumors. Moreover, GelMA-CJCNPs demonstrated satisfactory photodynamic antibacterial effects against *Staphylococcus aureus* infections, thereby promoting postsurgical wound healing. Hence, this immunotherapeutic hydrogel booster, as a facile and effective postoperative adjuvant, possesses a promising potential for inhibiting tumor recurrence and accelerating skin regeneration.

1. Introduction

Melanoma is a highly aggressive and rapidly metastatic cutaneous cancer with high rates of mortality [1]. In standard melanoma surgery, tumor tissues are removed by wide excision of peripheral healthy skin tissues to minimize the amount of residual malignant cells [2,3]. Nevertheless, the presence of invasive residual tumors increases the risk of local recurrence and micrometastasis, especially in resected high-risk stage II/III melanoma with a recurrence rate of up to 70 % [4]. Currently, to prevent tumor recurrence, immunotherapy has emerged as a postoperative adjuvant treatment by assisting patients in restoring and enhancing their immune functions [5]. However, the poor immunogenicity and immune evasion induced by an immunosuppressive tumor microenvironment (ITM) after surgery significantly impede the body's antitumor immune response [6–8]. In addition, the potential bacterial infection in excessively large wounds delays tissue repair and greatly

Peer review under responsibility of KeAi Communications Co., Ltd.
* Corresponding author.
** Corresponding author.
*** Corresponding author.
E-mail addresses: 1029193191@qq.com (W. Wu), chenjierong@gdph.org.cn (J. Chen), yuzq@smu.edu.cn (Z. Yu).
[1] These authors contributed equally to this work.

https://doi.org/10.1016/j.bioactmat.2024.08.028
Received 24 January 2024; Received in revised form 7 August 2024; Accepted 26 August 2024

increases the risk of postoperative complications [9,10]. Moreover, due to the essential difference between tumor and wound environments, synergistic treatment that impedes tumor recurrence and promotes wound repair remains a major clinical challenge. Therefore, developing a postoperative adjuvant for melanoma that can simultaneously amplify immunotherapy to efficiently eliminate residual tumor cells and inhibit bacterial infections to accelerate wound repair is imperative.

Photodynamic therapy (PDT) has emerged as an effective and minimally invasive approach for recurrent cancer treatment. The reactive oxygen species (ROS) generated by PDT can trigger immunogenic cell death (ICD), promoting the infiltration of cytotoxic T lymphocytes (CTLs) [11–14]. In addition, the ROS generated by PDT can oxidatively damage surrounding biomolecules, such as lipids, proteins, and nucleic acids, and thus has shown promise in combating bacterial infections [15,16]. However, tumor cells synthesize more glutathione (GSH) to eliminate excessive ROS by upregulating glutaminase (GLS) activity, which is involved in glutamine metabolism, thereby maintaining intracellular redox homeostasis [17–20]. Interestingly, glutamine metabolism plays a crucial role in the formation and progression of ITM. As the main component of ITM, immunosuppressive and protumoral M2-type tumor-associated macrophages (TAMs) depend more on glutamine metabolism compared to immunoreactive and tumoricidal M1-type TAMs, and glutamine normally accumulates in M2-type TAMs and promotes their polarization [21]. Additionally, GLS is less expressed in M1-type TAMs and more expressed in M2-type TAMs. Blocking glutamine metabolism using GLS inhibitors can not only prevent annihilation of the PDT-generated ROS to enhance tumor immunogenicity but also reduce M2-type TAMs polarization to reverse ITM, synergistically recruiting and activating CTLs. Undesirably, interferon-gamma (IFN-γ) secreted by CTLs upregulates the expression of programmed death ligand 1 (PD-L1) on the surface of tumor cells, which binds to programmed death 1 (PD-1) expressed on the surface of CTLs, eventually leading to the inactivation of CTLs and the development of adaptive immune resistance [22,23]. Previous reports have shown that JQ1, a small molecule inhibitor of bromodomain-containing protein 4 (BRD4), effectively reduces IFN-γ-induced PD-L1 expression to overcome inducible immune evasion, further sensitizing tumor cells to immunotherapy [24,25]. Therefore, the combination of PDT, GLS inhibitors, and JQ1 is a supplementary treatment for melanoma that simultaneously enhances the efficacy of postsurgical immunotherapy and antibacterial therapy.

To achieve a ternary synergistic effect, these agents need to be simultaneously delivered to the tumor site *via* nanoscale drug delivery systems (DDSs) [26,27]. Among these systems, the drug self-delivery systems (DSDSs) are efficient and safe drug delivery systems with great potential in the biomedical field [28]. These systems self-assemble from pure active drugs and have extremely high drug-loading capacities while avoiding adverse side effects caused by carriers [29]. In addition, based on the essential differences between tumor and wound microenvironments, it is urgent to design suitable wound dressings to synergistically achieve postoperative tumor treatment and wound healing. Recently, as intriguing platforms for the local delivery of immunomodulators and cells, hydrogels can provide an immunomodulatory microenvironment for the recruitment and activation of endogenous immune cells due to their tunable properties and diverse bioactivities [30]. Among them, methacrylic anhydride-modified gelatin (GelMA), which is biocompatible, biodegradable, and has adjustable physical properties promotes cell adhesion and proliferation, making it widely utilized in tissue engineering applications [31–34]. Therefore, integrating DSDSs with GelMA hydrogels to form a biomimetic platform can further leverage the merits of both components and serve as an effective postoperative adjuvant for inhibiting tumor recurrence and accelerating tissue repair.

Herein, an immunotherapeutic hydrogel booster (GelMA-CJCNPs) was developed as a postoperative adjuvant for tumor treatment and wound healing by incorporating ternary carrier-free nanoparticles (CJCNPs) containing chlorine e6 (Ce6), a BRD4 inhibitor (JQ1), and a GLS inhibitor (C968) into GelMA dressings (Scheme 1). Under laser irradiation, the GelMA-CJCNPs induced ROS production and GSH reduction to synergistically disrupt redox homeostasis, leading to the elimination of tumor cells and enhanced ICD effects. Subsequently, a cascade of immune responses, including the release of DAMPs, the maturation of dendritic cells (DCs), and the infiltration of CTLs, was activated. Additionally, GelMA-CJCNPs reduced M2-type TAMs polarization to remodel ITM by blocking glutamine metabolism, thereby further recruiting and activating CTLs. Furthermore, GelMA-CJCNPs downregulated IFN-γ-induced PD-L1 expression to mitigate acquired immune resistance, further sensitizing tumor cells to immunotherapy. The results demonstrated that GelMA-CJCNPs achieved synergistic effects in enhancing tumor immunogenicity and reversing ITM to prevent primary and distant tumor growth. Notably, this hydrogel booster also demonstrated remarkable photodynamic antibacterial effects against postoperative *Staphylococcus aureus* (*S.aureus*) infections, expediting the healing process of infected wounds. As a result, this multifunctional immunotherapeutic hydrogel booster provides a facile and effective adjunct platform for the postoperative management of melanoma.

2. Materials and methods

Synthesis and characterizations of CJCNPs. Firstly, Ce6, JQ1, and C968 were individually dissolved in DMSO at a 5 mg/mL concentration. Subsequently, the mixture of Ce6 (50.0 μL), JQ1 (33.6 μL), and C968 (39.9 μL) was dripped into the ddH_2O (2 mL) with continuous stirring for 15 min. After dialyzed (MWCO 1.0 kDa) with ddH_2O for 8 h, CJC nanoparticles (CJCNPs) were obtained.

The morphology and hydrodynamic size of CJCNPs were measured by a transmission electron microscope (TEM, JEOL, JEM-2100F) and a Malvern Zetasizer Nano ZS90 (Malvern). The absorption spectrum of CJCNPs was measured by a UV–vis spectrometer (UV-2450, Shimadzu). The drug loading efficiency of Ce6, JQ1, and C968 was recorded by a UV–vis spectrometer (UV-2450, Shimadzu) and high-performance liquid chromatography (HPLC) (Shimadzu, MD, USA).

Synthesis and characterizations of GelMA hydrogel. Methacrylic anhydride-modified gelatin (GelMA) was synthesized according to previous reports [35]. Dissolving 1.0 g of gelatin in 10 mL of PBS under stirring at 60 °C yielded a gel solution. Combining 0.85 mL of methacrylic anhydride with 2 mL of PBS formed a MA solution. This solution was then added dropwise to the aforementioned Gel solution under stirring and allowed to react in the dark at 55 °C for 3 h. The pH of the reaction solution was maintained between 8.0 and 9.0 throughout the reaction. Then, the reaction was halted by adding 60 mL of ddH_2O. The diluted reaction solution underwent dialysis in ddH_2O for 4 d, followed by lyophilization to obtain GelMA. Then, the photocuring precursor solution was prepared by dissolving 150 mg GelMA, 5 mg LAP, and 116.4 μg CJCNPs in 1 mL PBS solution. The GelMA-CJCNPs hydrogel is formed by shining 405 nm blue light for 1 min.

^1H NMR (Bruker 400 MHz Advance, Switzerland) of GelMA in D_2O was carried out to verify the methylacryloyl modification of gelatin. Scanning electron microscopy (SEM) (FEI Quanta 200, FEI Company, Czech Republic) was used to observe the microstructure of GelMA. The GelMA hydrogel compress-strain measurements were taken with a tensile-compressive tester (AGS-V universal testing machine with a 20 N sensor, Shimadzu Corporation) in press mode. Rheology was analyzed with a TA-DHR-2 (TA Instruments, United States).

Detection of intracellular GSH. B16F10 cells (5×10^5 cells) were seeded in 6-well plates and cultured for 12 h, followed by incubation with the different groups (Control, Ce6, JQ1, C968, CJCNPs) at the same Ce6 (5 μg/mL), JQ1 (2.7 μg/mL), and C968 (3.9 μg/mL) concentration. After 12 h incubation, the B16F10 cells were collected to determine the relative GSH ratio using a GSH assay kit.

Detection of intracellular ROS. B16F10 cells (5×10^5 cells) were seeded in 6-well plates and cultured for 12 h, followed by incubation

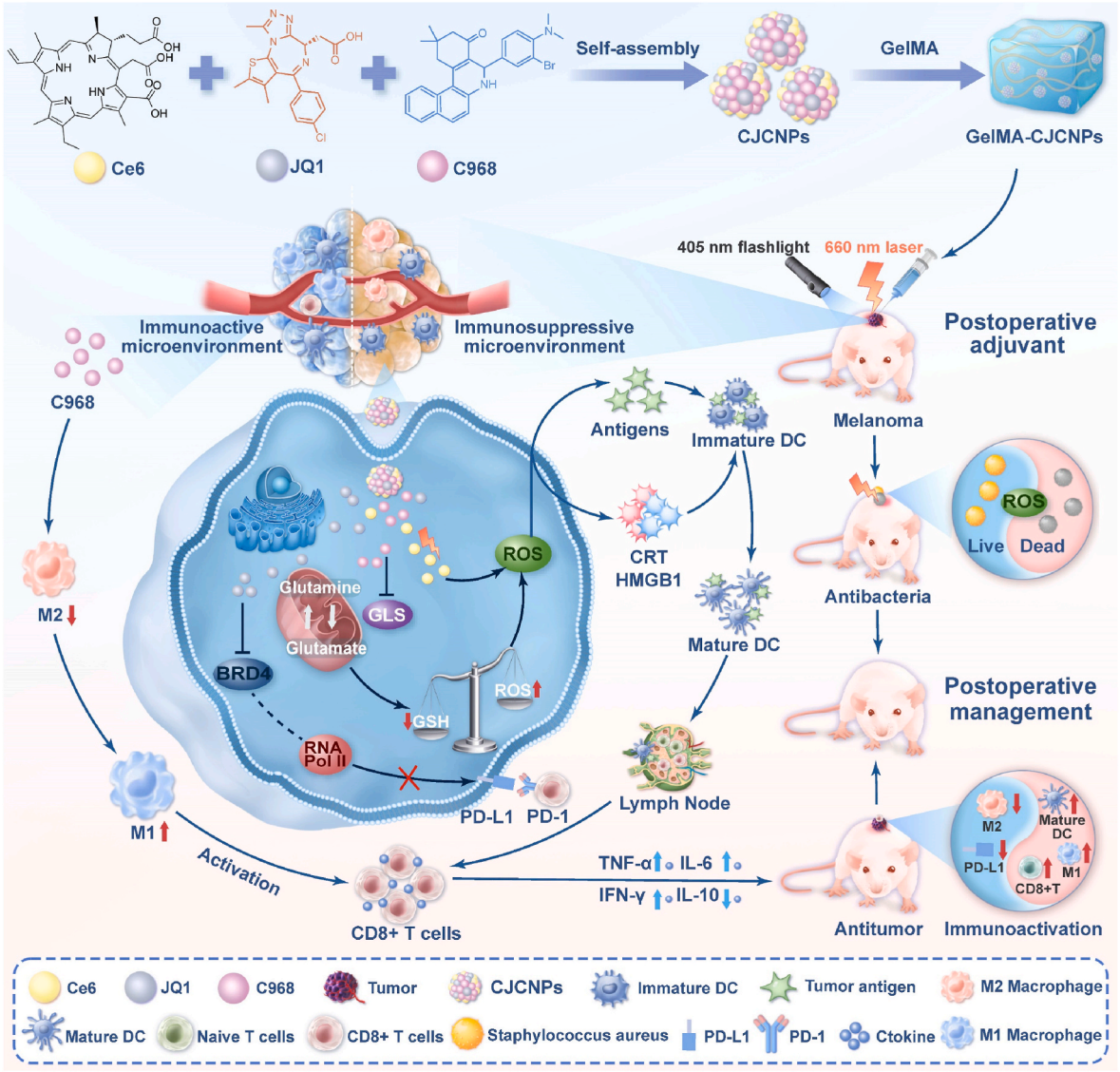

Scheme 1. Schematic illustration of the immunotherapeutic hydrogel booster (GelMA-CJCNPs) for inhibiting postoperative tumor recurrence and promoting wound healing.

with various formulations (Control, Ce6, JQ1, C968, CJCNPs, Ce6 (+), CJCNPs (+)) at the same Ce6 (5 μg/mL), JQ1 (2.7 μg/mL), and C968 (3.9 μg/mL) concentration for 12 h. Then a 660 nm laser (0.1 W/cm^2, 3 min) was used to irradiate B16F10 cells in the Ce6 (+) and CJCNPs (+) groups. All groups were washed with PBS and stained with DCFH-DA and DAPI to detect the intracellular generation of ROS by a fluorescence microscope.

Examination of PD-L1 expression *in vitro*. B16F10 cells were seeded into the 6-well plates (1×10^6 cells) and cultured for 12 h. Then, the B16F10 cells were incubated with control (PBS), JQ1, IFN-γ, JQ1 + IFN-γ, CJCNPs + IFN-γ at the same IFN-γ (100 ng/mL), Ce6 (5 μg/mL), JQ1 (2.7 μg/mL), C968 (3.9 μg/mL), and CJCNPs (11.64 μg/mL) concentrations for 12 h. Then the cells were collected to determine the expression of BRD4 and PD-L1 by Western blot analysis.

Immunofluorescence staining of CRT and HMGB1. B16F10 cells were seeded into the 6-well plates (5×10^5 cells) and cultured for 12 h. Then, the B16F10 cells were treated with Ce6 (5 μg/mL), Ce6 (+) (5 μg/mL), JQ1 (2.7 μg/mL), C968 (3.9 μg/mL), CJCNPs (11.64 μg/mL), or CJCNPs (+) (11.64 μg/mL) for 12 h. The cells in the groups requiring laser treatment (Ce6 (+) and CJCNPs (+) groups) were irradiated with a 660 nm laser (0.1 W/cm^2, 3 min). After 4 h of incubation, the cells were washed with PBS and fixed with 4 % paraformaldehyde (15 min). Then, the cells were incubated with ananti-careticulin antibody or anti-HMGB1 antibody overnight at 4 °C, followed by another incubation with a goat antirabbit IgG H&L. After 1 h, the cells were stained with DAPI for 20 min. Finally, the cell immunofluorescence of each group was observed by CLSM.

Evaluation of the antitumor effect of primary tumor-bearing mice model. B16F10 cells (1×10^6) were subcutaneously injected into C57BL/6 mice to establish a primary tumor-bearing mouse model. When the tumor volume reached about 50 mm^3, the mice were randomly divided into 7 groups, namely, the control, GelMA-Ce6, GelMA-JQ1, GelMA-C968, GelMA-CJCNPs, GelMA-Ce6 (+), and GelMA-CJCNPs (+) groups, in which the concentration of Ce6 remained consistent at 50 μg/mL. The GelMA-Ce6 (+) and GelMA-CJCNPs (+) groups were subjected to a 660 nm laser (0.1 W/cm^2, 10 min) on Days 1, 3, and 5. To simulate the clinical surgical treatment of melanoma, a circular wound (diameter: 8 mm) was established at the tumor site of mice. Subsequently, 100 μL PBS or hydrogel was applied to the wound site, and the hydrogel was formed *in situ* under 405 nm laser irradiation. The weights and tumor sizes of mice were measured every other day, and the calculation formula for tumor size was based on a previous

report [36]. The tumor tissue of each group was collected for histological analyses (H&E staining and TUNEL staining) and immunohistochemical staining (Ki67, CRT, and HMGB1). In addition, the normal tissues of mice were collected for H&E staining.

Immune cells analysis. Tumor tissues from the mice were taken for immune cell analysis. The tumor tissue of each group was cut into small pieces and digested with hyaluronidase (0.3 g/L), collagenase IV (0.5 g/L), and DNase (0.15 g/L) at 37 °C for 1 h. The cells were then filtered through a sieve (200 mesh) and centrifuged at 1200 rpm for 5 min. Subsequently, the cells were collected and stained with various antibodies for flow cytometry analysis. Matured DCs (stained with anti-CD11c-Qdot 605, anti-CD80-Pacific Blue, and anti-CD86-PE antibodies), infiltrating T lymphocytes (stained with anti-CD45-APC-Cy7, anti-CD11b-FITC, and anti-CD8-Cy5.5 antibodies) and TAMs (stained with anti-F4/80-PE-Cy7, anti-CD206-APC, and anti-CD86-PE antibodies) in each group were assessed through flow cytometry using a BD FACS machine. In addition, Frozen sections of tumor tissue were collected for immunohistochemical (M1 and M2) and immunofluorescent ($CD4^+$ T and $CD8^+$ T) analysis by CLSM. Immunohistochemical staining was performed with anti-iNOS and anti-CD206 antibodies and immunofluorescent staining was performed with anti-CD8-FITC, anti-CD4-PE antibodies, and DAPI.

RNA-sequencing analysis. When the tumor volume reached approximately 50 mm^3, the mice were randomly divided into 2 groups ($n = 3$), including the control and GelMA-CJCNPs (+) groups. On the 7th day after tumor treatment, tumor tissues from the control and GelMA-CJCNPs (+) groups were frozen in liquid nitrogen for 5 min. The RNA-sequencing analysis of tumors was performed by Guangzhou Kedio Biotechnology Co., Ltd. (Guangzhou, China). The differential analysis between two groups of genes was conducted using the R package "edgeR", $p < 0.05$ and $|\text{Fold change}| > 1.2$ are considered significant. Gene ontology (GO) analysis and Kyoto Encyclopedia of Genes and Genomes (KEGG) analysis were performed with the "clusterProfiler" package. Finally, the R package "ggplot2" was used for plotting.

Evaluation of the antitumor effect of the bilateral tumor-bearing mice model. To induce a bilateral B16F10 tumors model, B16F10 cells (1×10^6) were subcutaneously implanted on the left rear of the back, followed by the same number of cells on the right 6 days later. When the left tumor volume reached approximately 50 mm^3, the C57BL/6 mice were randomly divided into 7 groups ($n = 5$), including the control, GelMA-Ce6, GelMA-JQ1, GelMA-C968, GelMA-CJCNPs, GelMA-Ce6 (+), and GelMA-CJCNPs (+) groups. To simulate clinical surgery for melanoma, a circular wound with a diameter of 8 mm was made at the left tumor site, and a hydrogel was applied to the wound site. The weights and bilateral tumor volumes of the mice were measured every other day. At the end of the treatment, all mice were sacrificed, and tumor tissues were collected, photographed, and weighed. In addition, the levels of tumor necrosis factor-α (TNF-α), interferon-γ (IFN-γ), interleukin-6 (IL-6), and interleukin-10 (IL-10) in serum samples were determined by enzyme-linked immunosorbent assay (ELISA).

***In vivo* infected wound healing.** A circular wound with a diameter of 8 mm was established on the back of C57BL/6 mice, and clinically isolated Staphylococcus aureus (50 μL, 1×10^7 CFU mL^{-1}) was inoculated into the wound to establish an infection model. The mice were then randomly divided into three groups, including the control, GelMA-CJCNPs, and GelMA-CJCNPs (+) group, with 5 mice in each group. The GelMA-CJCNPs group was treated with a 405 nm laser to form a hydrogel *in situ*, and the GelMA-CJCNPs (+) group was treated with a 660 nm laser (0.1 W/cm^2, 10 min) after hydrogel formation. Thereafter, mice were kept in individual cages for 10 days. The wound areas of each group were photographed and measured (days 0, 1, 4, 7, and 10). On the 10th day, the skin tissue from mice was collected for H&E and Masson staining analysis.

In addition, the number of residual bacteria in the skin tissue was examined to verify the antibacterial effect of the GelMA-CJCNPs under laser irradiation. On Day 5 after treatment, the wound tissues of mice treated with PBS, GelMA-CJCNPs, or GelMA-CJCNPs (+) were collected to extract microorganisms (10 mg/mL). After a 100-fold dilution with PBS solution, 100 μL of the diluted solution was spread on a solid LB agar plate, and the colonies were counted following a 24-h incubation at 37 °C.

Statistical analysis. All data were presented as mean ± standard deviation (SD). The two-tailed *t*-test was used for two-group comparisons and ordinary one-way ANOVA was used for multiple group comparisons. *$P < 0.05$; **$P < 0.01$; ***$P < 0.001$.

3. Results and discussions

Synthesis and characterization of CJCNPs and GelMA hydrogel. The photosensitizer Ce6 molecule has the potential to interact with a variety of hydrophobic chemotherapeutic agents because of its hydrophobic conjugated skeleton [37,38]. The interactions among Ce6, JQ1, and C968 in the aqueous phase led to the formation of a carrier-free nanomedicine (CJCNPs) *via* self-assembly using the nanoprecipitation method. (Fig. 1a). Various feeding ratios of Ce6, JQ1, and C968 were designed to achieve the ideal nanoparticle, whose morphology and sizes were assessed through transmission electron microscopy (TEM) and dynamic light scattering (DLS) (Fig. 1b and Fig. S1). The TEM images of the CJCNPs revealed that Ce6, JQ1, and C968 self-assembled into uniform spherical nanoparticles at a 1: 1: 1 feeding ratio, and the hydrated particle size was 98 ± 3.9 nm according to the DLS experiment. The stability and potential of the carrier-free nanomedicine were also examined. Results demonstrated that at various feeding ratios, the potential and particle size did not change noticeably over a period of several days (Figs. S2 and S3). Therefore, carrier-free nanomedicines with a feed ratio of 1: 1: 1 were selected as the CJCNPs for subsequent experiments. The diameter of CJCNPs increased slightly but remained stable overall in the presence of 10 % fetal bovine serum (FBS) compared to that of CJCNPs in water, which might be due to the formation of protein crowns on the surface of the nanoparticles (Fig. S4). The drug loading efficiency (DLE) of CJCNPs was studied by UV–vis spectroscopy and high-performance liquid chromatography (HPLC) (Fig. S5). The results showed that the DLE of Ce6, JQ1, and C968 were 42.94 %, 23.33 %, and 33.72 %, respectively.

To understand the self-assembly mechanism of CJCNPs, the molecular dynamics (MD) simulations were investigated (Fig. S6a). Ce6, JQ1, and C968 molecules (mole ratio: 1:1:1) were randomly inserted into a simulation box ($x = 7.0$ nm, $y = 7.0$ nm, and $z = 7.0$ nm) and subjected to 20 ns of MD simulation. As shown in Fig. S6b the molecules in the CJCNPs system accumulated continuously under the intermolecular interaction with the process of simulation, and finally formed assemblies. The intermolecular interactions between the three drug molecules were analyzed to further investigate the driving forces during the self-assembly process of CJCNPs. The hydroxyl group of Ce6 formed a series of hydrogen bonds with the carbonyl oxygen atom of JQ1 and C968, respectively; the secondary amine group in C968 formed a series of hydrogen bonds with the carbonyl oxygen atom of Ce6 and JQ1, respectively; and the hydroxyl group of JQ1 formed a series of hydrogen bonds with the carbonyl oxygen atom of Ce6 and C968, respectively (Fig. S6c). Meanwhile, π–π stacking was induced by conjugated ring structures in Ce6, JQ1, and C968 (Fig. S6d). Collectively, molecular dynamics simulation analysis showed that the dominant forces in the CJCNPs system were hydrogen bonding and π-π stacking. Furthermore, the characterization of the UV–vis absorption spectra under different conditions was carried out to investigate the potential self-assembly mechanism of the CJCNPs. The characteristic absorption peak of Ce6 recovered upon adding dimethyl sulfoxide (DMSO) solution, providing that the intermolecular noncovalent interactions CJCNPs were destroyed (Fig. 1c). The addition of hydrophobic sodium dodecyl sulfate (SDS) caused a change in the characteristic absorption peak of CJCNPs, providing additional evidence for the involvement of hydrophobic

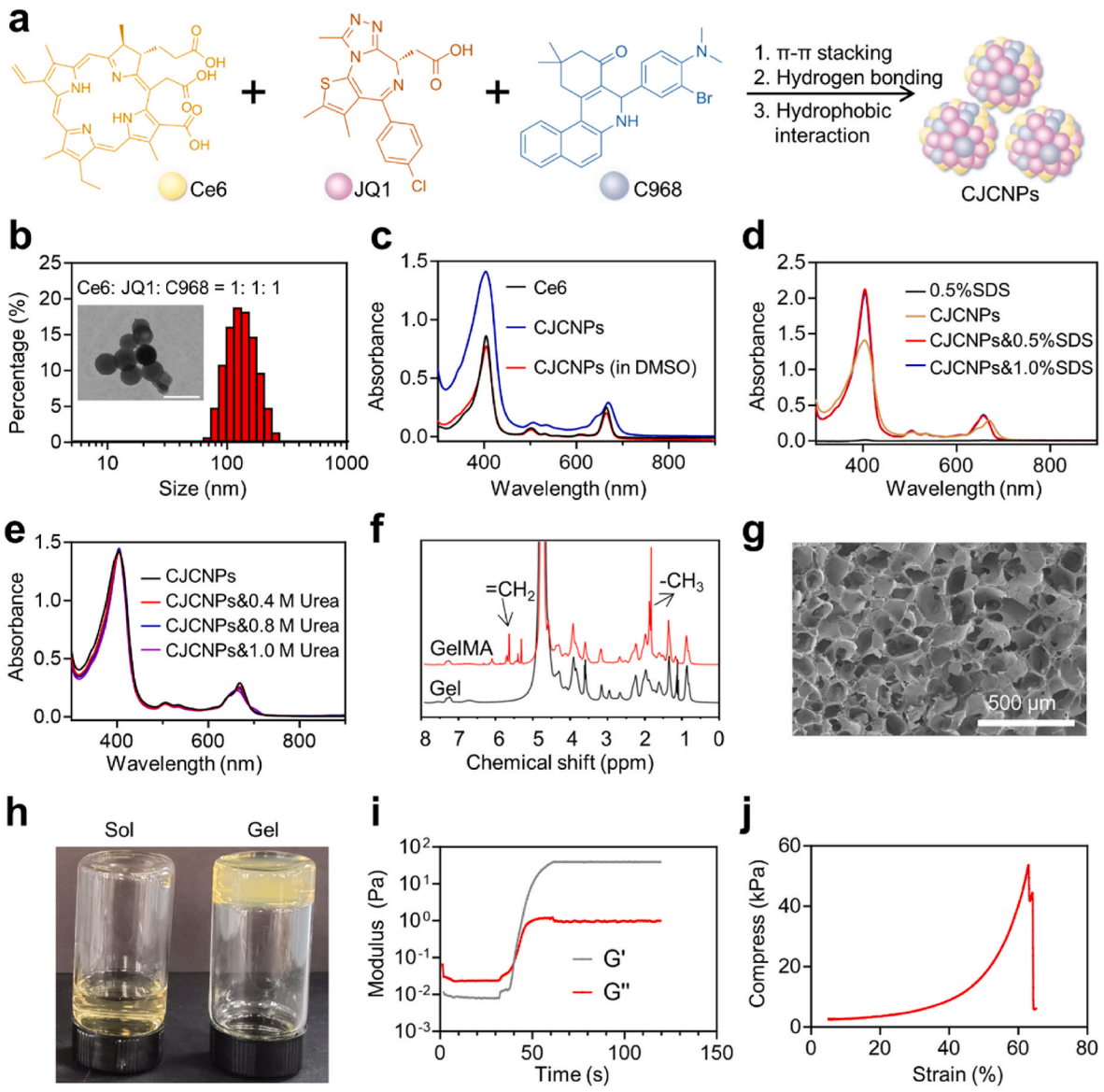

Fig. 1. Preparation and characterization of CJCNPs and GelMA hydrogel. (a) Schematic illustration of Ce6, JQ1, and C968 self-assembling into CJCNPs through π-π stacking and hydrophobic interactions. (b) Hydrodynamic size and TEM image (insert) of CJCNPs at the feeding ratio of 1: 1: 1. Scale bar: 200 nm. (c) UV–vis absorbance spectrum of CJCNPs in the presence or absence of DMSO. (d) UV–vis absorbance spectrum of CJCNPs in the presence or absence of SDS (0.5 % and 1.0 %, w/v). (e) UV–vis absorbance spectrum of CJCNPs in the presence or absence of Urea (0.4, 0.8, and 1.0 M). (f) ^{1}H NMR spectra of GelMA in D_2O. (g) SEM of lyophilized GelMA hydrogel. (h) Sol and gel photographs of GelMA hydrogel. (i) A dynamic time-sweep rheological analysis of GelMA hydrogel. (j) The mechanical properties of GelMA hydrogel.

interactions in the self-assembly process (Fig. 1d). The absorption spectra of CJCNPs changed obviously after incubation with Urea solutions, indicating that the hydrogen bonding was also one of the main driving forces for drug self-assembly (Fig. 1e). Nevertheless, when dispersed in 1.0 M sodium chloride (NaCl) solutions, the self-assembly of CJCNPs remained undisturbed, indicating that electrostatic interactions were not the predominant driving force for the formation of CJCNPs (Fig. S7). In summary, the self-assembly process of CJCNPs primarily relies on hydrophobic, π−π interactions, and hydrogen bonding.

The GelMA hydrogel is a biocompatible and biodegradable material with a wide range of biomedical applications [39]. The ^{1}H NMR spectra confirmed that methacrylic anhydride (MA) was successfully conjugated to the gelatin (Gel), as new peaks occurred at "-CH_3" and " = CH_2" (Fig. 1f). The lyophilized GelMA hydrogels had a porous structure according to the SEM results, which was favorable for drug delivery and metabolite expulsion (Fig. 1g). Fig. 1h shows the sol-gel transformation of GelMA after 405 nm flashlight irradiation, indicating successful synthesis of the GelMA hydrogel. According to the results of the dynamic time-sweep rheological analysis, GelMA could be light-cured in less than 50 s after being exposed to a 405 nm laser at an irradiation dose of 30 mW/cm^2 (Fig. 1i). In addition, the viscosity of GelMA changes little over time (Fig. S8). The compressive strength of the GelMA hydrogel was approximately 53.5 kPa, indicating that it has good compressive properties (Fig. 1j). Furthermore, an immunotherapeutic hydrogel booster was developed by incorporating CJCNPs into GelMA hydrogel dressings. Then, the stability of CJCNPs after incorporation into hydrogel was studied by analyzing the particle size. As shown in Fig. S9, CJCNPs incorporated into the hydrogel showed no significant change in particle size over a period of several days, indicating that the incorporation into hydrogels did not result in particle aggregation. To investigate whether the addition of nanoparticles affects the stability of the hydrogels, the physicochemical properties of GelMA-CJCNPs were further analyzed.

The equilibrium swelling rate of hydrogels was similar before and after the addition of CJCNPs (Fig. S10a). Both GelMA and GelMA-CJCNPs can achieve sol-gel conversion after irradiation by a 405 nm flashlight (Fig. S10b). The compressive strength of GelMA-CJCNPs was approximately 40 kPa, which was similar to that of GelMA (Fig. S10c). These results indicated that nanoparticle doping has little effect on the characteristics of the hydrogel. As one of the most important properties of tissue adhesives, the adhesion, and durability of the hydrogel were characterized by the pig skin adhesion test. Herein, GelMA-CJCNPs were immersed in PBS for 48 h to simulate a harsh wet environment. Before soaking, GelMA-CJCNPs were stuck firmly to the pig skin and stretched, twisted, and bent. After soaking for 48 h, GelMA-CJCNPs not only adhered firmly to the skin, but could be stretched, twisted, and bent without shedding (Fig. S11).

***In vitro* antitumor efficacy.** Motivated by the above findings, we conducted additional experiments on CJCNPs at the cellular level. According to recent research findings, free Ce6 displays a limited capacity to enter cells, and nanoscale DDSs are considered to enhance drug internalization within cells [40,41]. The cellular uptake of free Ce6 and CJCNPs was assessed based on the Ce6 fluorescence intensity using a Confocal laser scanning microscopy (CLSM) (Fig. 2a). The red color of cells incubated with CJCNPs was stronger than that of cells incubated

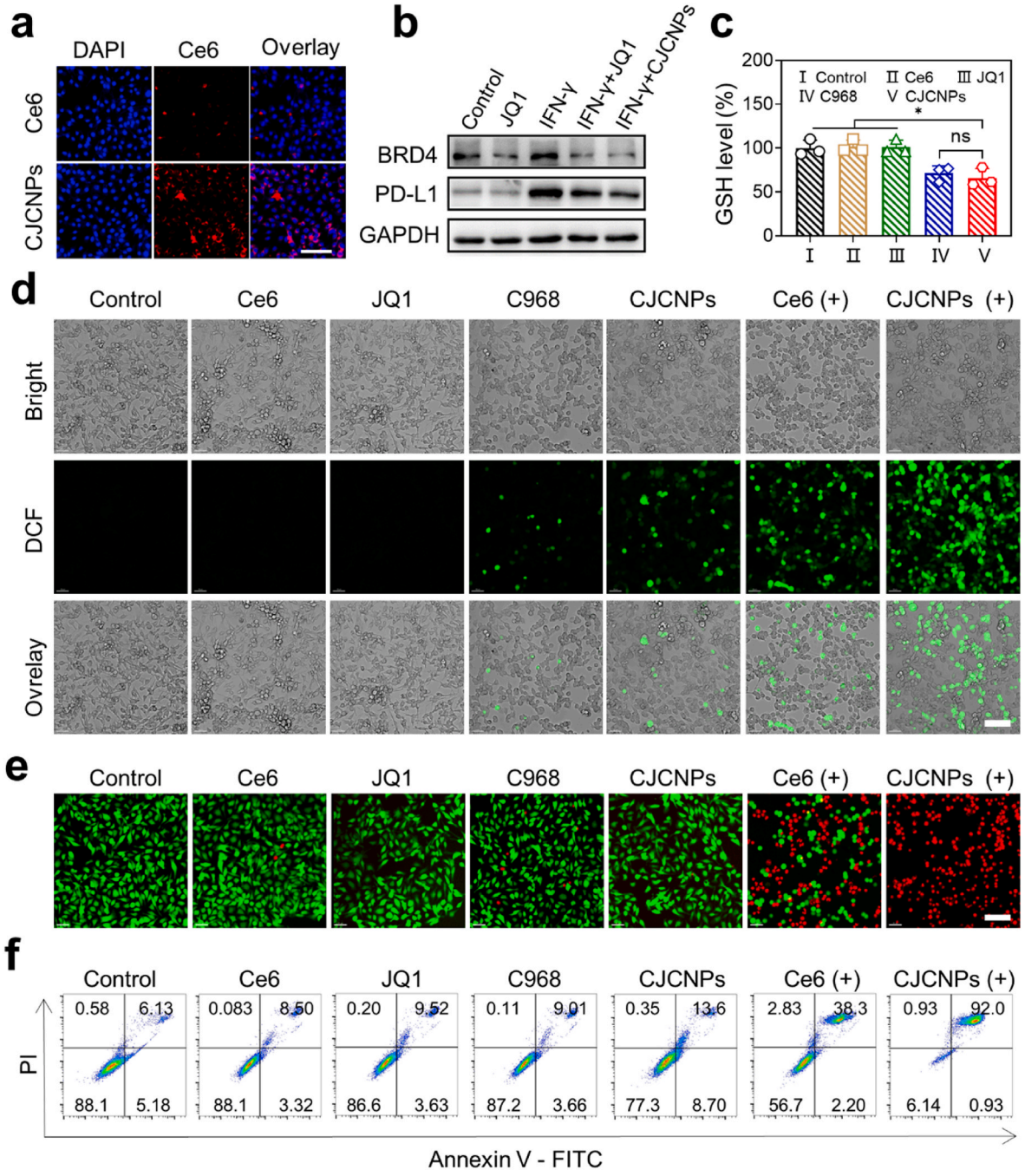

Fig. 2. *In vitro* cell study of CJCNPs. (a) CLSM of the intracellular uptake analysis. Scale bar: 100 μm. (b) Western-blot assay of BRD4 and PD-L1 expression in B16F10 cells upon different treatments *in vitro*. (c) GSH level of B16F10 cells after various treatments. (d) CLSM images of intracellular ROS production of B16F10 cells in the presence or absence of light irradiation after treatment with Ce6, JQ1, C968, or CJCNPs. Scale bar: 100 μm. (e) Live/dead cell staining of B16F10 cells after treatment with Ce6, JQ1, C968, or CJCNPs in the presence or absence of light irradiation. Scale bar: 100 μm. (f) Annexin V-FITC/Propidium iodide (PI) apoptosis detection of B16F10 cells after various treatments. *P < 0.05.

with free Ce6, indicating that enhanced cellular uptake was achieved when Ce6 was self-assembled into nanoparticles. As a BRD4 inhibitor, JQ1 has been previously proven to inhibit the expression of PD-L1 induced by IFN-γ. Western blot analysis confirmed that both free JQ1 and CJCNPs effectively inhibited the upregulation of PD-L1 induced by IFN-γ in B16F10 cells (Fig. 2b and Fig. S12). Previous research has shown that C968 can inhibit GLS activity to interfere with glutamine metabolism, resulting in reduced GSH synthesis. Our study revealed that compared with the control treatment, both C968 and CJCNPs significantly reduced the GSH level in B16F10 cells, to approximately 71.13 % and 66.02 %, respectively (Fig. 2c). Ce6, another component of CJCNPs, can generate reactive oxygen species under light radiation, thereby inducing photodynamic therapy. The photodynamic characteristics of the CJCNPs were determined using 2′,7′-dichlorodihydrofluorescein diacetate (DCFH-DA) as a sensor, which is oxidized by ROS to DCF that can produce green fluorescence. The fluorescence signals of the Ce6 (+) and CJCNPs (+) groups increased upon exposure to 660 nm laser radiation, demonstrating that a significant amount of ROS was produced by these cells (Fig. 2d and Fig. S13). Additionally, green fluorescence signals were observed in the cells treated with C968 and CJCNPs, due to the oxidative stress induced by the reduction of intracellular GSH. More importantly, the fluorescence intensity of cells in the CJCNPs (+) group was higher than that in the Ce6 (+) group, which was attributed to enhanced cellular uptake and reduced GSH production. Therefore, CJCNPs (+) amplified intracellular oxidative stress by reducing intracellular GSH levels and increasing intracellular ROS generation in B16F10 cells, showing great potential in tumor treatment.

Encouraged by the increase in intracellular oxidative stress, the *in vitro* antitumor effects of the CJCNPs were further assessed. First, the cytotoxicity of CJCNPs on B16F10 cells was investigated using a Cell Counting Kit 8 (CCK8) assay. Ce6 alone exhibited limited inhibition of tumor cell proliferation, regardless of light irradiation, possibly due to inadequate cell internalization (Fig. S14). In contrast, the cytotoxicity of the CJCNPs was significantly enhanced upon light exposure, highlighting the immense potential of the self-assembled delivery strategy in tumor treatment. Additionally, the antitumor efficacy of the CJCNPs was assessed using a live/dead cell staining assay. The results showed that unilluminated B16F10 cells displayed bright green fluorescence, indicating that there was no obvious damage to the cells in the absence of PDT (Fig. 2e). Conversely, PDT conducted on the Ce6 (+) and CJCNPs (+) groups induced cell death, as indicated by the red fluorescence upon laser irradiation. Notably, the CJCNPs (+) group exhibited the strongest red fluorescence, indicating its robust antitumor capability. Subsequently, cell apoptosis was further evaluated using Annexin V-FITC/Propidium iodide (PI) staining (Fig. 2f and Fig. S15). Notably, the CJCNPs (+) group exhibited the most potent apoptosis-inducing effect, indicating the most potent apoptosis-inducing effect. These results demonstrated that CJCNPs can effectively induce apoptosis in tumor cells under laser irradiation, thus providing a basis for subsequent *in vivo* antitumor experimental investigations.

ICD effect and DCs maturation. Previous studies suggest that PDT can induce ICD effect, initiating a series of immunological cascades [42,43]. Calreticulin (CRT) and high mobility group box 1 (HMGB1) are widely acknowledged as two pivotal biomarkers in the cascades of ICD [44,45]. CRT is exposed from the endoplasmic reticulum (ER) to the cell membrane surface as an "eat me" signal, while HMGB1 migrates from the nucleus as a "find me" signal, promoting immature DCs and macrophages to phagocytose dying tumor cells and their debris and subsequently recruiting toxic T lymphocytes. The *in vitro* ICD effect was investigated by immunofluorescence staining of CRT and HMGB1 on B16F10 cells after being subjected to various treatments. Fig. 3a shows that the Ce6 (+) and CJCNPs (+) groups exhibited significant fluorescence signals, suggesting that the administration of PDT to these two groups upregulated the expression of CRT on the cell membrane. Interestingly, the CJCNPs (+) group exhibited brighter green fluorescence than the Ce6 (+) group, demonstrating superior CRT ectropion. In contrast, the immunofluorescence intensity of HMGB1 in the CJCNPs (+) group decreased due to the release of extracellular HMGB1(Fig. 3b). These results indicated that the CJCNPs (+) group induced superior CRT ectropion and HMGB1 secretion, indicating an enhanced ICD effect. This difference may be attributed to enhanced cellular uptake and reduced GSH production. Furthermore, the addition of C968 to CJCNPs prevented the ROS from being annihilated by GSH through the inhibition of glutamine metabolism, which could amplify intracellular oxidative stress and ultimately enhance tumor immunogenicity.

Encouraged by the promising ICD effect of CJCNPs *in vitro*, we subsequently incorporated them into GelMA physically, creating an immunotherapeutic hydrogel booster (GelMA-CJCNPs) aimed at evaluating the *in vivo* expression of CRT and HMGB1. Immunohistochemical staining of tumor tissues from B16F10 tumor-bearing mice effectively assessed two crucial ICD effect indicators: CRT exposure and HMGB1 secretion (Fig. 3c). Immunohistochemical signals corresponding to the appearance of CRT and the disappearance of HMGB1 were observed in the CJCNPs (+) group, confirming the membranal exposure of CRT and the extracellular release of HMGB1. These findings affirmed the induction of the ICD effect through enhanced oxidative stress and its potential to enhance antitumor immunotherapy. We subsequently investigated DCs maturation within tumor tissues after various treatments. GelMA-CJCNPs (+) group showed a significantly greater proportion of mature $CD80^{+}CD86^{+}$ DCs (34.5 ± 2.1 %) in the lymph nodes than did the PBS group (12.9 ± 2.7 %), which was approximately 2.7-fold greater than the number of mature DCs (Fig. 3d and e). These results indicated that this hydrogel booster has the potential to enhance ICD effect to promote DC maturation, further supporting its role in enhancing antitumor immune responses.

***In vivo* antitumor efficacy of the primary tumor model.** Encouraged by the promising *in vitro* antitumor effects of CJCNPs, their antitumor capabilities were further investigated *in vivo*. As depicted in Fig. 4a, to simulate the clinical scenario of surgical melanoma treatment, we generated 8 mm diameter skin wounds at the tumor site in C57BL/6 mice. Subsequently, we randomly applied PBS, GelMA-Ce6, GelMA-JQ1, GelMA-C968, GelMA-CJCNPs, GelMA-Ce6 (+), or GelMA-CJCNPs (+) to the wounds. According to the tumor growth curve, the average tumor volume of mice treated with PBS showed an increase to 850 mm^3 over 16 days, whereas the average tumor volume of mice treated with GelMA-CJCNPs (+) was effectively suppressed to 70 mm^3 (Fig. 4b and c). The GelMA-CJCNPs (+) group exhibited stronger tumor suppression than the GelMA-Ce6 (+) group, possibly attributed to the synergistic antitumor effect of GelMA-CJCNPs (+) in boosting tumor immunogenicity and reversing ITM. In addition, the GelMA-CJCNPs (+) group had smaller tumor volume and tumor weight than GelMA-CJC (+) group, indicating that GelMA-CJCNPs (+) exhibited stronger tumor inhibition (Fig. S16). Tumor tissues of each group after treatments were subsequently weighed to investigate the therapeutic effect. The average tumor weight in the GelMA-CJCNPs (+) group was 0.03 ± 0.04 g, which was lower than that in the PBS group (0.50 ± 0.06 g), further indicating that GelMA-CJCNPs (+) showed considerable superiority in inhibiting tumor growth (Fig. 4d). Furthermore, the biosafety of GelMA-CJCNPs is a major concern. Fig. 4e shows that following GelMA-CJCNPs treatment, there was no significant change in the body weight of mice, indicating good biocompatibility of GelMA-CJCNPs. Moreover, histological analysis (H&E) of normal tissues revealed that GelMA-CJCNPs did not cause apparent side effects and instead showed great biocompatibility (Fig. S17). Additionally, blood routine tests were carried out after the collection of blood samples from mice. No significant changes in blood routine markers were noted in the GelMA-CJCNPs (+) group when compared to the control group, further indicating the biocompatibility of the hydrogel booster (Fig. S18).

To delve more profoundly into the antitumor mechanism of GelMA-CJCNPs, the histopathological analysis on tumor tissues after different treatments was performed using H&E, terminal deoxynucleotidyl transferase dUTP nick-end labeling (TUNEL), and Ki67 stainings,

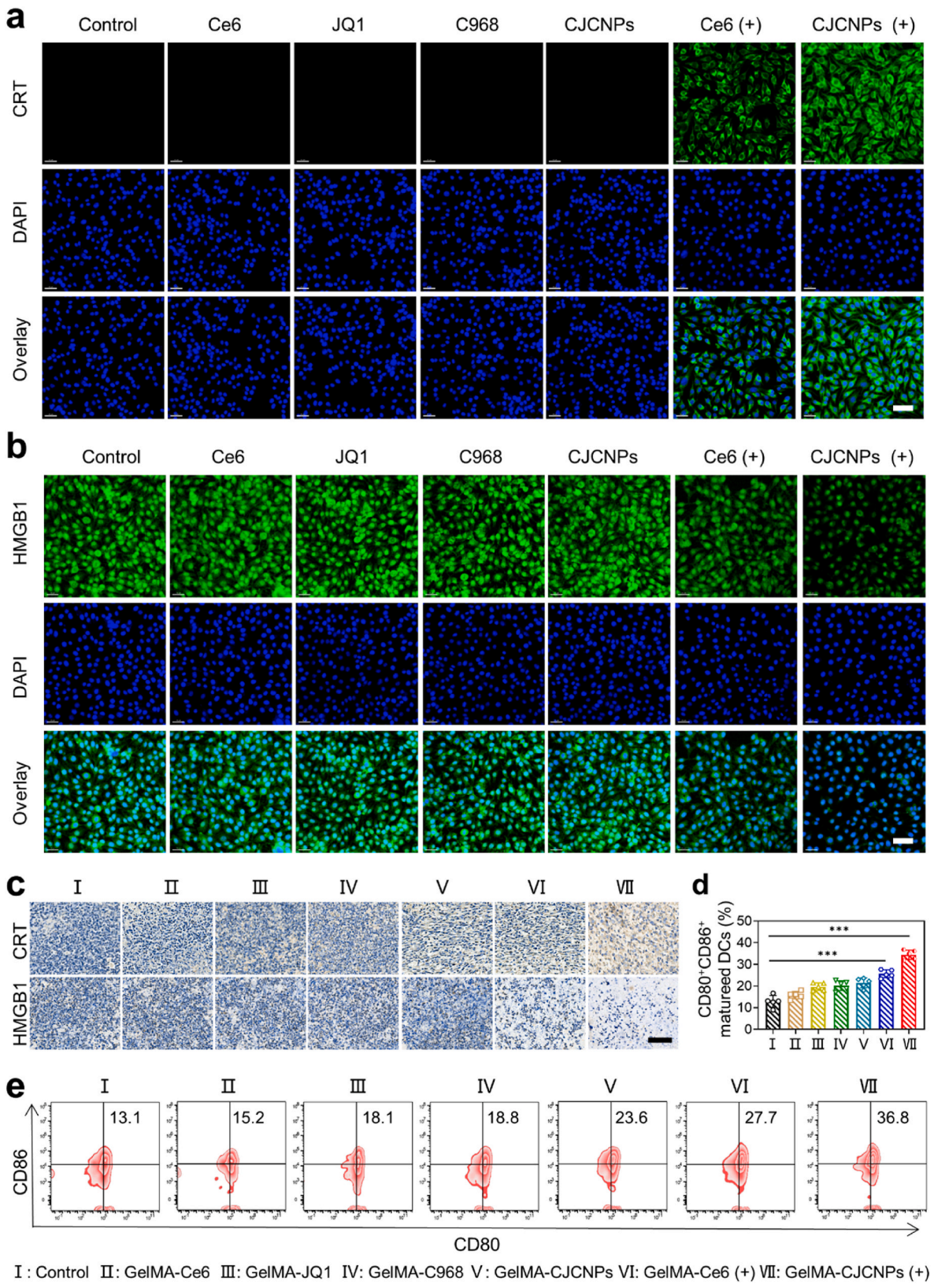

Fig. 3. *In vitro* and *in vivo* enhanced ICD effect and DCs maturation. CRT (a) and HMGB1 (b) immunofluorescence staining of B16F10 cells after treatment with Ce6, JQ1, C968, or CJCNPs in the presence or absence of light irradiation. Scale bar: 50 μm. (c) CRT and HMGB1 immunohistochemistry staining of tumor tissues after different treatments. Scale bar: 100 μm. (d) Quantitative analysis of DCs maturation. (e) Flow cytometry analysis of DCs maturation in tumor tissues. ***$P < 0.001$.

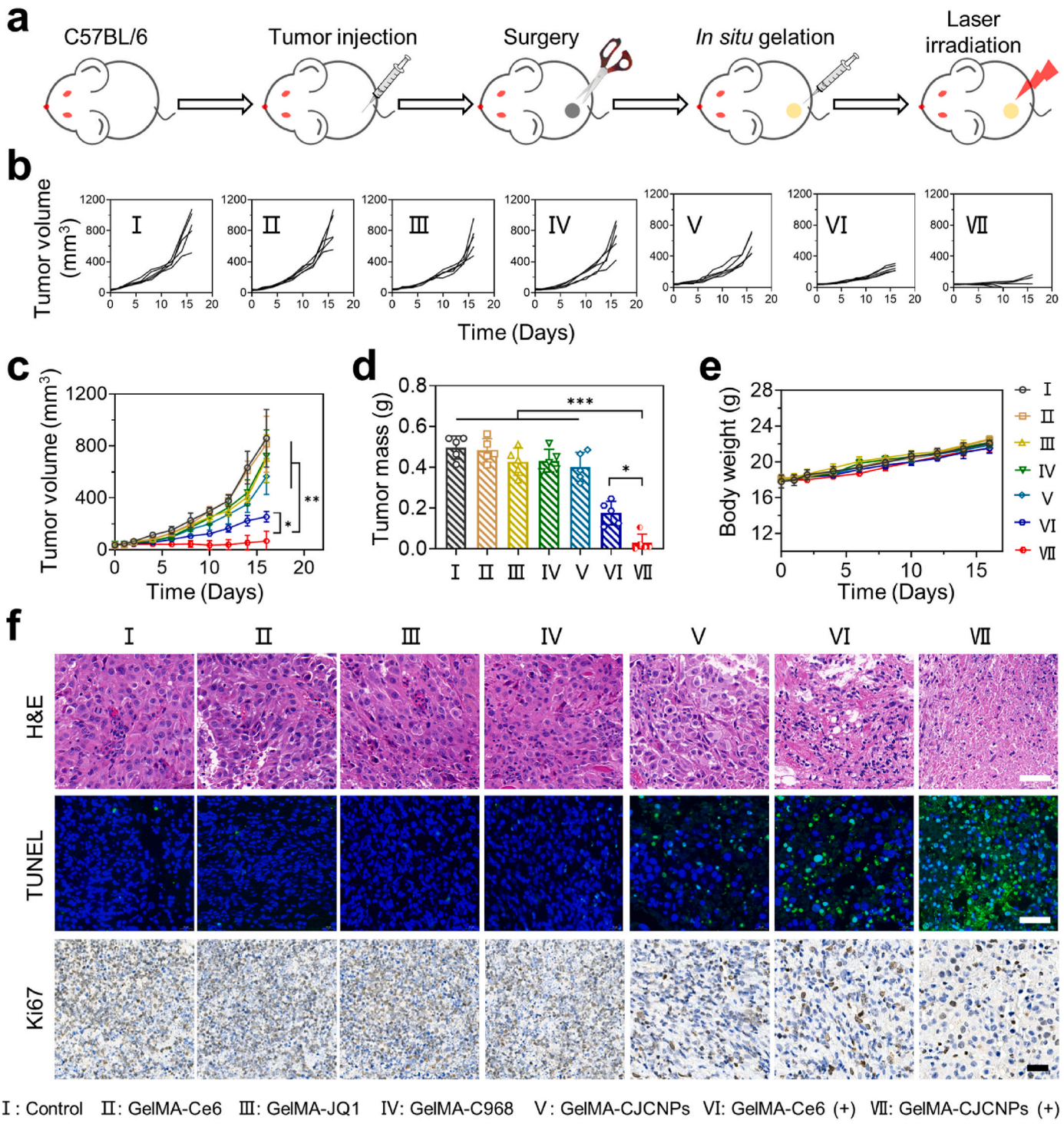

Fig. 4. Therapeutic efficacy of GelMA-CJCNPs (+) on B16F10 tumor-bearing mice. (a) Schematic illustration of synergistic treatment studies. B16F10 tumor-bearing mice were injected with different solutions directly at the tumor site, followed by irradiation using a 405 nm flashlight to induce *in situ* gel formation, and subsequently underwent laser irradiation as a treatment. (b) Tumor-growth curves of individual animals. Average tumor-growth curves (c), tumor mass (d), and body weights (e) of the mice in different treatment groups. (f) H&E staining, TUNEL immunofluorescence staining, and Ki67 immunohistochemistry staining of tumor tissues after different treatments. Scale bar: 50 μm *P < 0.05; **P < 0.01; ***P < 0.001.

(Fig. 4f). H&E staining revealed extensive damage to the tumor tissue in the GelMA-CJCNPs (+) group, with nuclei exhibiting no apparent morphological features. Additionally, the strongest apoptotic signals were observed in the TUNEL-stained images, and the lowest number of Ki67-positive cells was observed in the tumor tissue after being treated with GelMA-CJCNPs (+). In summary, the results indicated that GelMA-CJCNPs when exposed to laser irradiation, maximized the synergistic therapeutic effect and exhibited excellent inhibition of tumor growth.

***In vivo* evaluation of immune activation effect.** To delve deeper into understanding the mechanisms driving the effectiveness of anti-tumor immunotherapy, immunological cascade processes were explored in the B16F10 tumor model, with a specific focus on TAMs polarization, PD-L1 regulation, and tumor-infiltrating T cells. C968 is believed to reprogram the tumor metabolic microenvironment by inducing

glutamine deprivation, thereby decreasing M2-type TAMs and increasing M1-type TAMs [6,46]. To assess TAMs polarization, we utilized flow cytometry (FCM) analysis, which targeted the CD86, CD206, and F4/80biomarkers. There was a notable increase in M1-type TAMs and a significant decrease in M2-type TAMs in both the GelMA-CJCNPs and GelMA-CJCNPs (+) groups (Fig. 5a–d). Specifically, the M1/M2 TAMs ratios of the GelMA-CJCNPs and GelMA-CJCNPs (+) groups were increased to 5.3 ± 1.9 and 4.5 ± 0.6, which were 7.8 and 6.6 times greater than those of the PBS group (0.68 ± 0.11), respectively (Fig. S19). In addition, immunohistochemical analysis demonstrated that GelMA-CJCNPs induced an increase in M1-type TAMs (iNOS signaling) and a decrease in M2-type TAMs (CD206 signaling) in the presence and absence of laser irradiation (Fig. 5e). These results verify that C968 in GelMA-CJCNPs has the potential to promote the polarization of TAMs, thereby reprogramming ITM by regulating glutamine metabolism. Inspired by the fact that GelMA-CJCNPs (+) can promote DC maturation, subsequently presenting tumor-specific antigens to T lymphocytes, the tumor-infiltrating CTLs were detected using the FCM

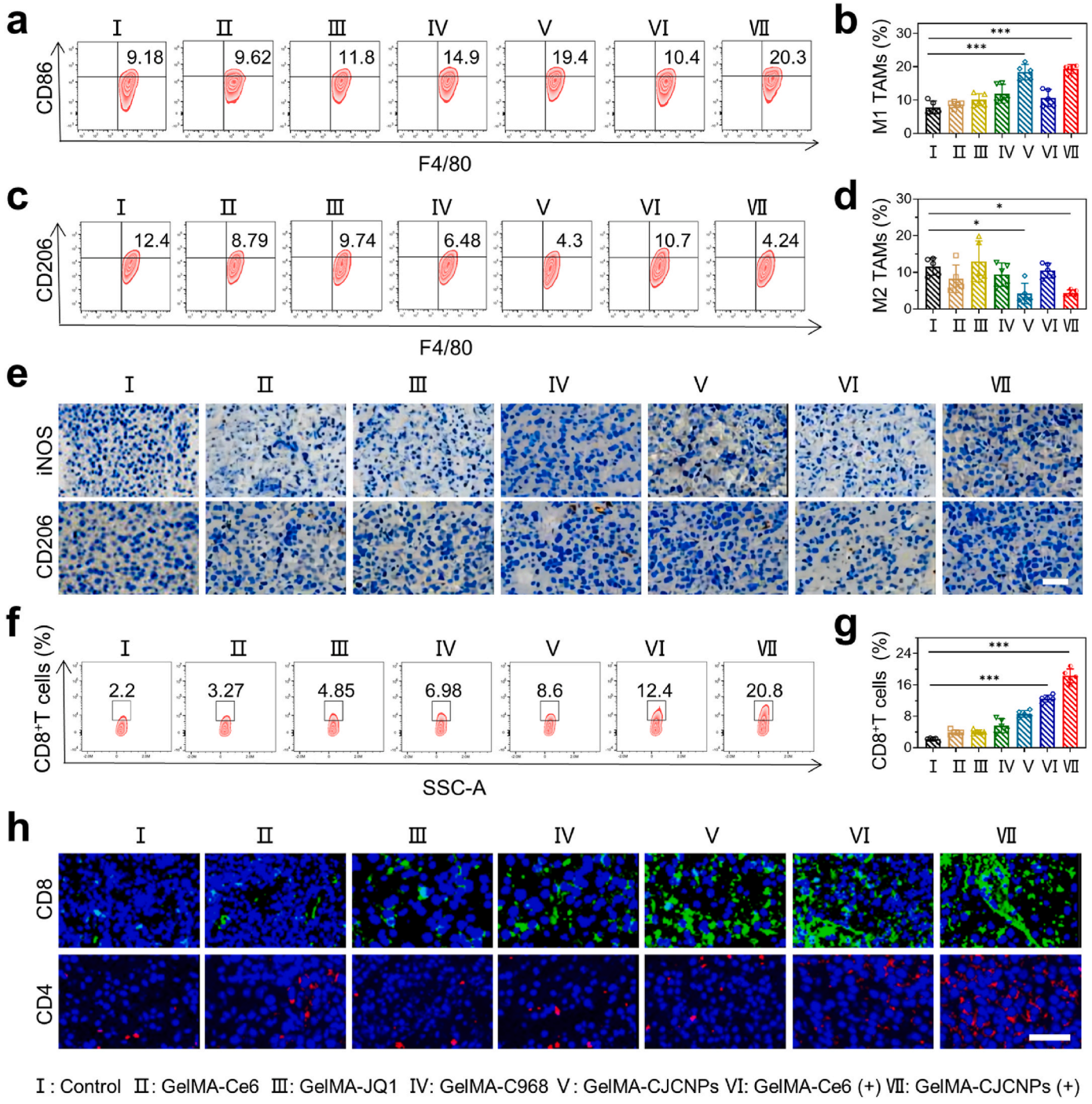

Fig. 5. Immune activation effect of GelMA-CJCNPs (+) on the B16F10 tumor-bearing mice. (a) Flow cytometry analysis of the percentages of M1-type phenotypes TAMs in the tumor tissues. (b) Quantitative analysis of M1-type TAMs. (c) Flow cytometry analysis of the percentages of M2-type phenotypes TAMs in the tumor tissues. (d) Quantitative analysis of M2-type TAMs. (e) The immunohistochemistry staining of TAMs polarization in the tumor tissues. (f) Flow cytometry analysis of infiltrating $CD8^+$ T cells in tumor tissues from the mice after various treatments. (g) Quantitative analysis of $CD8^+$ T cells. (h) The immunofluorescence staining of $CD8^+$ and $CD4^+$ T cells in the tumor tissues. Scale bar: 50 μm *P < 0.05; ***P < 0.001.

method in the B16F10 tumor model. As shown in Fig. 5f and g, GelMA-CJCNPs (+) group increased $CD8^+$ T cells proportion to 18.3 ± 1.8 %, 8.5-fold greater than that of the control group, indicating that the hydrogel booster activated the antitumor immune response. Additionally, immunofluorescence analysis revealed a substantial increase in $CD8^+$ T cell infiltration (green fluorescence) and $CD4^+$ T cell infiltration (red fluorescence) in tumor tissues from the mice treated with GelMA-CJCNPs (+), indicating the potent ability of GelMA-CJCNPs (+) to maximally activate both $CD8^+$ and $CD4^+$ T cells for activating systemic antitumor immune response (Fig. 5h). However, interferon-γ (IFN-γ) secreted by tumor-infiltrating CTLs can upregulate the expression of PD-L1 on the surface of tumor cells, which binds to PD-1 on the surface of CTLs, leading to adaptive immune resistance [47]. Therefore, avoiding CTLs-inducible immune evasion is crucial for enhanced immunotherapy. To further evaluate whether GelMA-CJCNPs suppressed IFN-γ-inducible immune evasion *in vivo*, the expression of PD-L1

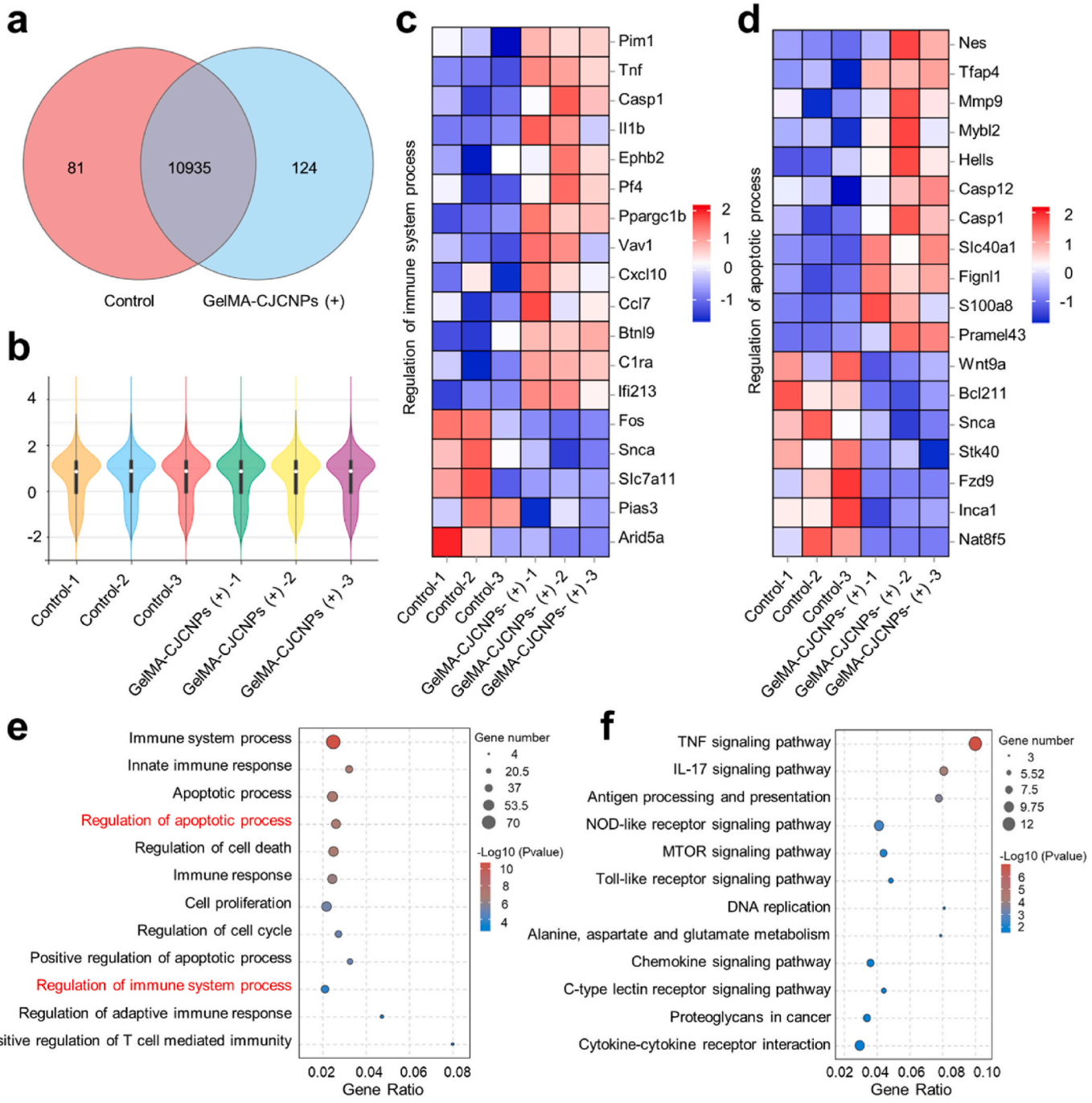

Fig. 6. Antitumor mechanism study with RNA-sequencing. (a) The Venn of gene counts in the control and GelMA-CJCNPs (+) groups. The intersection area represents the genes that are present in both control and GelMA-CJCNPs (+) groups. (b) The violin diagram of gene counts in the control and GelMA-CJCNPs (+) groups to understand the distribution and variability of gene expression data. (c) The heat map of the differential expression related to the regulation of the immune system process following treatment with the control and GelMA-CJCNPs (+) groups. (d) The heat map of the differential expression related to the regulation of the apoptotic process following treatment with the control and GelMA-CJCNPs (+) groups. Red indicates high expression, blue indicates low expression, and white indicates medium expression. (e) The GO pathways analysis of the differentially expressed genes to find that these genes are concentrated in some specific biological processes. (f) The KEGG pathways analysis of the differentially expressed genes to discuss the biological pathways affected by GelMA-CJCNPs (+) groups.

in the tumor tissues was examined using immunohistochemical staining (Fig. S20). The immunohistochemical findings showed a decrease in PD-L1 expression in the three groups containing JQ1, including the GelMA-JQ1, GelMA-CJCNPs, and GelMA-CJCNPs (+) groups. These results indicated that GelMA-CJCNPs effectively counteracted IFN-γ-induced PD-L1 upregulation, thereby overcoming acquired immune resistance. In brief, GelMA-CJCNPs have the potential to reactivate T cells-mediated immunotherapy by increasing the tumor immunogenicity, reversing immunosuppressive tumor microenvironment through tumor-selective metabolic reprogramming, and preventing PD-1/PD-L1 recognition by decreasing the expression of PD-L1.

RNA-sequencing analysis. To further elucidate the potential biological mechanism of the immunotherapeutic hydrogel booster, RNA sequencing analysis was conducted on tumor tissues from the control and GelMA-CJCNPs (+) groups. Quality control of the samples ensures that the sequencing depth is consistent and the genes sequenced by different groups are highly overlapping (Fig. 6a and b). The transcription of 11,140 genes was detected in the collected tumors, of which 81 and 124 genes were uniquely transcribed in the PBS- and GelMA-CJCNPs (+)-treated tumors, respectively. By analyzing the genes differentially expressed between the various groups, we discovered that in the tumor tissues treated with GelMA-CJCNPs (+), 146 genes were upregulated (red dots) and 96 genes were downregulated (yellow dots) (Fig. S21). Immune-related genes, specifically those associated with the "Regulation of immune system process" and "Regulation of apoptotic process" were further screened to assess the antitumor immune response. The functional association network of immune-related genes is shown in Fig. S22. The results demonstrated significant differences in the expression of multiple immune-related and apoptotic-related genes between the two groups (Fig. 6c and d). Specifically, the expression of Tnf, Casp1, and Cxcl10 was upregulated by GelMA-CJCNPs under laser irradiation, suggesting that GelMA-CJCNPs (+) induced ICD effects and thus activated the immune response [48–50]. The increase in the mRNA levels of Nes, Tfap4, Mmp9, and Mybl2, which are related to apoptosis, indicated that compared with the control treatment, GelMA-CJCNPs (+) induced the most pronounced increase in apoptosis [51–54]. To further demonstrate the ability of GelMA-CJCNPs to modulate both the immune response and apoptosis pathways, Gene Ontology (GO) analysis and Kyoto Encyclopedia of Genes and Genomes (KEGG) analysis were performed. GO analysis indicated that the GelMA-CJCNPs (+) had an impact on the Immune system process, Apoptotic process, Regulation of apoptotic process, Regulation of adaptive immune response, and Positive regulation of T cell mediated immunity (Fig. 6e). The results showed that the GelMA-CJCNPs (+) group elicited a robust immune response and stimulated CTLs activation, consistent with the *in vivo* experimental results. Furthermore, KEGG pathway analysis demonstrated the induction of immune response-related pathways by GelMA-CJCNPs, including the TNF signaling pathway, the IL-17 signaling pathway, and the Toll-like receptor signaling pathway (Fig. 6f). Overall, these results demonstrated that GelMA-CJCNPs under laser irradiation could regulate the tumor immune microenvironment, which is highly beneficial for enhancing the effect of antitumor immunotherapy.

***In vivo* antitumor effects of the bilateral tumor-bearing model.** The systemic antitumor effects of GelMA-CJCNPs were further investigated through sequential injection of B16F10 cells to establish a bilateral tumor-bearing model (Fig. 7a). GelMA-CJCNPs were directly photocured onto the wound site of the primary tumor on the right side, followed by a 660 nm laser irradiation to initiate systemic antitumor immunity. The progression of primary and distant tumors was tracked to evaluate the systemic antitumor effect. As shown in Fig. 7b, mice treated with GelMA-Ce6 (+) had an average tumor volume of 280 mm^3, while mice treated with PBS showed rapid tumor growth, reaching an average tumor volume of 1060 mm^3 on the 16th day. Interestingly, the GelMA-CJCNPs (+) group had the most significant tumor inhibition effect with an average tumor volume of approximately 30 mm^3. In addition, all tumors from mice subjected to various treatments were collected and weighed to assess the antitumor effect of the immunotherapeutic hydrogel booster. Mice receiving GelMA-CJCNPs (+) treatment exhibited the lowest tumor weight (0.02 ± 0.05 g), which was approximately 1/25, 1/7, and 1/21 of that of mice receiving PBS treatment (0.54 ± 0.03 g), GelMA-Ce6 (+) treatment (0.15 ± 0.05 g), and GelMA-CJCNPs treatment (0.44 ± 0.05 g), respectively (Fig. 7c and d). Moreover, the distant tumor volumes of the mice treated with the different agents were also monitored (Fig. 7e). Similarly, the average tumor volume in the control group increased to 590 mm^3 after 16 days, whereas it was markedly inhibited to 110 mm^3 after treatment with GelMA-CJCNPs (+), suggesting a significant suppression of distant tumors in the GelMA-CJCNPs (+) group. Consistent results were also observed from tumor images and tumor weights (Fig. 7f and g). Specifically, the average tumor weight in the control group was nearly 0.44 ± 0.03 g, whereas, in the GelMA-CJCNPs (+) group, it was approximately 0.23 ± 0.04 g, further indicating that GelMA-CJCNPs had considerable ability to inhibit tumor growth under laser irradiation. In addition, there was no significant change in the body weight of mice receiving various treatments, suggesting that the GelMA-CJCNPs possess biological safety (Fig. S23). Overall, these results suggested that the GelMA-CJCNPs exhibited systemic antitumor immunity under laser irradiation to maximize the synergistic therapeutic effect without causing damage to the mice.

To further explore the antitumor mechanism of GelMA-CJCNPs in bilateral tumor models, the histopathological analysis on tumor tissues after different treatments was performed using H&E (Fig. 7h). H&E staining showed that the cell nuclei of bilateral tumor tissues in GelMA-CJCNPs (+) group had no obvious morphological characteristics, indicating that GelMA-CJCNPs exhibited excellent inhibition of tumor growth under laser irradiation. Then, the systemic antitumor immunity of GelMA-CJCNPs + L has been further evaluated. As shown in Fig. S24, the proportion of $CD8^+$ T cells in distant tumors reached 37.3 ± 7.6 % in the GelMA-CJCNPs (+) group, which was 2.2 times higher than that in the PBS group (17.0 ± 3.0 %). GelMA-CJCNPs effectively enhanced the infiltration and activation of $CD8^+$ T cells in distant tumors under laser irradiation and activated systemic immunostimulatory effect. In addition, to elucidate the potential mechanisms of antitumor immunotherapy of GelMA-CJCNPs (+) treatment, serum samples were collected from mice to evaluate the levels of cytokine release, including tumor necrosis factor-alpha (TNF-α), IFN-γ, interleukin-6 (IL-6), and interleukin-10 (IL-10) using an enzyme-linked immunosorbent assay (ELISA) (Fig. 7i). It was observed that GelMA-CJCNPs (+) significantly promoted the secretion of TNF-α, IFN-γ, and IL-6, 2.7-, 2.0-, and 1.8-fold greater than that in the control group, respectively, indicating that a synergistic immunotherapeutic strategy with a hydrogel booster elicited a remarkable inflammatory response. In addition, the decreased secretion of IL-10 was detected after treatment with GelMA-CJCNPs (+), which contributed to TME reprogramming.

***In vivo* wound healing study.** Potential bacterial infection after tumor surgery can significantly aggravate skin wound ulceration, limiting the application of repair materials in the postoperative treatment of melanoma. For the postoperative treatment of skin wounds, the ability of hydrogel materials to inhibit bacterial infection and facilitate wound healing is also important apart from cancer therapy. To confirm the effectiveness of GelMA-CJCNPs in promoting wound healing *in vivo* through photodynamic antibacterial activity, we conducted an experiment in which *S.aureus* infected skin wound (8 mm diameter) was afflicted on the backs of C57BL/6 mice to simulate postoperative infection commonly observed in clinical settings (Fig. 8a). The infected wounds were treated with *in situ* formed GelMA-CJCNPs and subsequently irradiated with a 660 nm laser. Compared with the control and GelMA-CJCNPs groups, the GelMA-CJCNPs (+) group had a smaller scar area and exhibited superior ability in wound healing (Fig. 8b). After 10 days, the wound closure rate of the GelMA-CJCNPs (+) group was approximately 98.5 %, which was significantly greater than that of the control group (82.6 %) and GelMA-CJCNPs group (82.9 %) (Fig. 8c). In

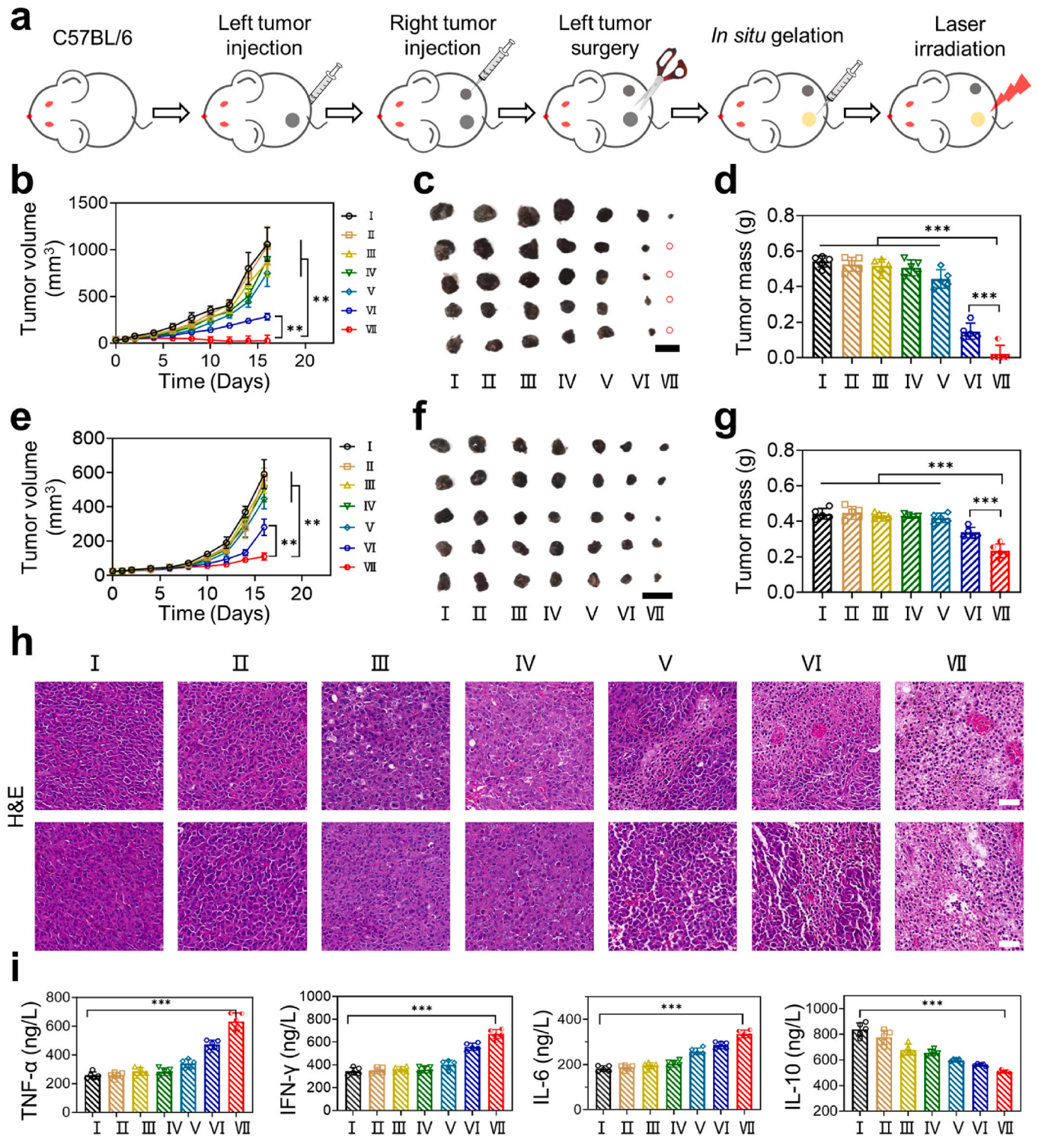

Fig. 7. Therapeutic efficacy of GelMA-CJCNPs (+) on the B16F10 bilateral tumor-bearing mice. (a) Schematic illustration of synergistic treatment studies. The bilateral tumor-bearing model was established by sequential injection of B16F10 cells. The B16F10 tumor-bearing mice were injected with different solutions directly at the left tumor site, followed by irradiation using a 405 nm flashlight to induce *in situ* gel formation, and subsequently underwent laser irradiation as a treatment. (b) The primary tumor volume changes in the mice after different treatments. Primary tumor images (c) and average tumor mass (d) of the mice at the end of treatments. Scale bar: 2 cm. (e) The distant tumor volume changes in the mice after different treatments. Distant tumor images (f) and average tumor mass (g) of the mice at the end of treatments. Scale bar: 2 cm. (h) H&E staining of bilateral tumor tissues (upper: primary tumor, bottom: distal tumor) after different treatments. Scale bar: 50 μm. (i) ELISA analysis of tumor necrosis factor-α (TNF-α), interferon-γ (IFN-γ), interleukin-6 (IL-6), and interleukin-10 (IL-10) in serum from mice after various treatments. $^{**}P < 0.01$; $^{***}P < 0.001$.

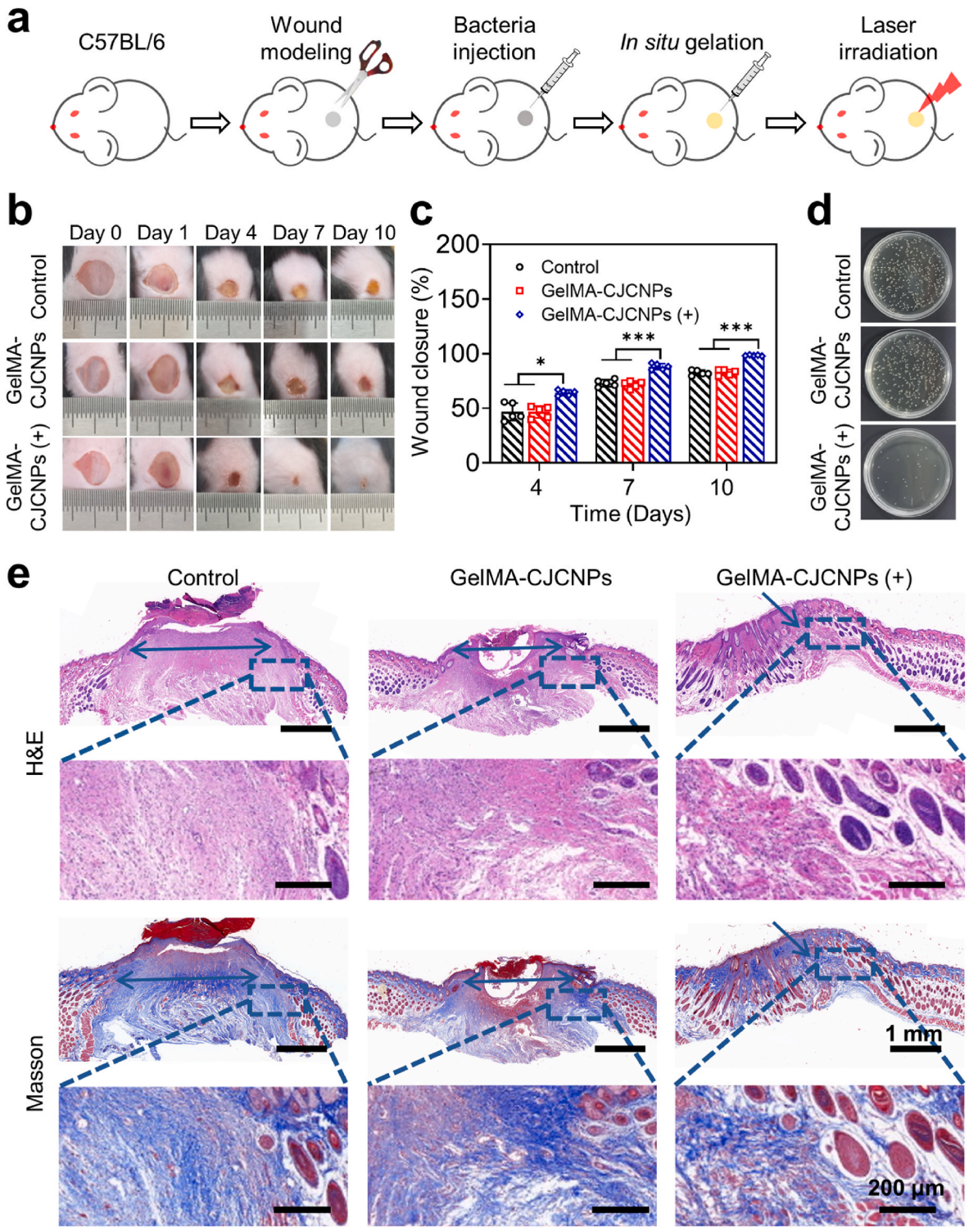

Fig. 8. *In vivo* therapeutic effect of GelMA-CJCNPs for infected wound healing. (a) Schematic illustration of *S. aureus*-infected wound healing. Representative photographs of wound (b) and wound closure rates (c) after various treatments at days 0, 1, 4, 7, and 10. (d) Residual bacteria from *S. aureus*-infected wound sites on Day 5. (e) H&E and Masson stainings of the wound healing regions on Day 10 for the control, GelMA-CJCNPs, and GelMA-CJCNPs (+) groups. *P < 0.05; ***P < 0.001.

addition, the GelMA-CJCNPs (+) group also had better wound healing compared to the GelMA-CJC (+) group (Figs. S25a and b). To assess the remaining bacteria at the wound site after treatment, skin tissue samples were collected from each group on Day 5. The experimental results demonstrated that the GelMA-CJCNPs (+) group had markedly lower levels of residual bacteria than the other groups (Fig. 8d, Fig. S25c, d, and Fig. S26). On Day 10, wound tissues were collected for H&E and Masson staining (Fig. 8e). The GelMA-CJCNPs (+) group exhibited noticeable regeneration of hair follicles, indicating that the hydrogel booster actively promoted the recovery of *S.aureus*-infected skin and exhibited a robust photodynamic antibacterial effect. To investigate whether GelMA-CJCNPs hydrogel causes damage to normal tissues, the

morphology of normal skin from mice was also detected *via* hematoxylin and eosin (H&E) staining and Masson staining. As shown in Fig. S27, compared with PBS treatment, there were no pathological changes in the normal skin of mice after receiving GelMA-CJCNPs (+) treatment, indicating the *in vivo* safety of the application of GelMA-CJCNPs.

4. Conclusion

In summary, an immunotherapeutic hydrogel booster (GelMA-CJCNPs) was successfully created by incorporating ternary carrier-free CJCNPs into GelMA dressings, which effectively suppressed tumor growth and promoted wound repair for the postoperative treatment of melanoma. GelMA-CJCNPs prevented the neutralization of PDT-generated ROS by inhibiting glutamine metabolism to amplify intracellular oxidative stress, resulting in profound cell death and enhanced ICD effects. Moreover, GelMA-CJCNPs reversed the immunosuppressive tumor microenvironment by reducing M2-type TAMs polarization and inhibited PD-L1-mediated immune resistance by blocking the IFN-γ-BRD4-PD-L1 axis. As expected, GelMA-CJCNPs suppressed the growth of proximal and distal tumors by eliciting systemic antitumor immune responses. Genome-wide analysis of tumor tissues *via* RNA sequencing also validated the impact of the amplified immune response induced by GelMA-CJCNPs. Notably, GelMA-CJCNPs facilitated postsurgical wound healing in the presence of inhibiting *S. aureus* infection. Overall, these results provide important insights into the development of a post-operative adjuvant for melanoma management to address some clinical challenges associated with surgery, including tumor recurrence prevention and resection-induced wound repair. In future work, several critical areas need to be addressed to further discuss the clinical translatability and future directions of this platform. First, ensuring the safety and biocompatibility of GelMA-CJCNPs through comprehensive preclinical and early-stage human trials is critical for clinical applications. Integration into clinical practice also requires seamless integration of hydrogel applications with surgical workflows. Future directions include deeper mechanistic studies to understand immune regulation, and exploring the combination of GelMA-CJCNPs with other therapeutic modalities such as immune checkpoint inhibitors and targeted therapies to enhance antitumor efficacy.

Ethics approval and consent to participate

All animal experiments and care were carried out in accordance with protocols approved by the Regional Ethics Committee for Animal Experiments at Shenzhen Bay Laboratory (Permit No. AERL202204).

CRediT authorship contribution statement

Yuanyuan Yang: Writing – review & editing, Writing – original draft, Methodology, Funding acquisition, Formal analysis, Conceptualization. **Bo Zhang:** Software, Investigation, Formal analysis. **Yangtao Xu:** Methodology, Formal analysis, Data curation. **Wenxiang Zhu:** Methodology, Data curation. **Zinian Zhu:** Resources, Investigation. **Xibo Zhang:** Resources, Investigation. **Wenze Wu:** Supervision. **Jierong Chen:** Writing – review & editing, Supervision. **Zhiqiang Yu:** Supervision, Project administration, Funding acquisition, Conceptualization.

Declaration of competing interest

The authors declare that they have no known competing financial interests or personal relationships that could have appeared to influence the work reported in this paper.

Acknowledgments

This work was supported by the National Natural Science Foundation of China (82372115 and 52073139), the China Postdoctoral Science Foundation (2023M731571), Dongguan Science and Technology of Social Development Program (20231800900322 and 20231800900362), the Postdoctoral Research Project Start-Up Funding of Dongguan People's Hospital (319341), the Guangdong Basic and Applied Basic Research Foundation (2023B1515120084 and 2023A1515110016), and the Training Program of National Natural Science Foundation of Dongguan People's Hospital (Z202402).

Appendix A. Supplementary data

Supplementary data to this article can be found online at https://doi.org/10.1016/j.bioactmat.2024.08.028.

References

[1] A. Tasdogan, B. Faubert, V. Ramesh, J.M. Ubellacker, B. Shen, A. Solmonson, M. M. Murphy, Z. Gu, W. Gu, M. Martin, S.Y. Kasitinon, T. Vandergriff, T.P. Mathews, Z. Zhao, D. Schadendorf, R.J. DeBerardinis, S.J. Morrison, Metabolic heterogeneity confers differences in melanoma metastatic potential, Nature 577 (7788) (2020) 115–120.

[2] C.C. Xue, M.H. Li, L. Sutrisno, B.B. Yan, Y. Zhao, Y. Hu, K.Y. Cai, Y. Zhao, S.H. Yu, Z. Luo, Bioresorbable scaffolds with biocatalytic chemotherapy and in situ microenvironment modulation for postoperative tissue repair, Adv. Funct. Mater. 31 (20) (2021) 2008732.

[3] R.N. Amaria, M. Postow, E.M. Burton, M.T. Tetzlaff, M.I. Ross, C. Torres-Cabala, I. C. Glitza, F. Duan, D.R. Milton, K. Busam, L. Simpson, J.L. McQuade, M.K. Wong, J. E. Gershenwald, J.E. Lee, R.P. Goepfert, E.Z. Keung, S.B. Fisher, A. Betof-Warner, A.N. Shoushtari, M. Callahan, D. Coit, E.K. Bartlett, D. Bello, P. Momtaz, C. Nicholas, A. Gu, X. Zhang, B.R. Korivi, M. Patnana, S.P. Patel, A. Diab, A. Lucci, V.G. Prieto, M.A. Davies, J.P. Allison, P. Sharma, J.A. Wargo, C. Ariyan, H. A. Tawbi, Neoadjuvant relatlimab and nivolumab in resectable melanoma, Nature 611 (7934) (2022) 155–160.

[4] A.M.M. Eggermont, C.U. Blank, M. Mandalà, G.V. Long, V.G. Atkinson, S. Dalle, A. M. Haydon, A. Meshcheryakov, A. Khattak, M.S. Carlino, S. Sandhu, J. Larkin, S. Puig, P.A. Ascierto, P. Rutkowski, D. Schadendorf, R. Koornstra, L. Hernandez-Aya, A.M.D. Giacomo, A.J.M.V.D. Eertwegh, J.J. Grob, R. Gutzmer, R. Gutzmer, P. C. Lorigan, A.C.J.V. Akkooi, C. Krepler, N. Ibrahim, S. Marreaud, M. Kicinski, S. Suciu, C. Robert, Adjuvant pembrolizumab versus placebo in resected stage III melanoma (EORTC 1325-MG/KEYNOTE-054): distant metastasis-free survival results from a double-blind, randomised, controlled, phase 3 trial, Lancet Oncol. 22 (5) (2021) 643–654.

[5] P. Li, Y. Xie, J. Wang, C. Bao, J. Duan, Y. Liu, Q. Luo, J. Xu, Y. Ren, M. Jiang, J. Li, H. Guo, H. Zhao, G. Wang, Y. Liang, W. Lu, Gene engineered exosome reverses T cell exhaustion in cancer immunotherapy, Bioact. Mater. 34 (2024) 466–481.

[6] Z. Mai, J. Zhong, J. Zhang, G. Chen, Y. Tang, W. Ma, G. Li, Z. Feng, F. Li, X.J. Liang, Y. Yang, Z. Yu, Carrier-free immunotherapeutic nano-booster with dual synergistic effects based on glutaminase inhibition combined with photodynamic therapy, ACS Nano 17 (2) (2023) 1583–1596.

[7] T.F. Gajewski, H. Schreiber, Y.X. Fu, Innate and adaptive immune cells in the tumor microenvironment, Nat. Immunol. 14 (10) (2013) 1014–1022.

[8] Y. Wang, Z. Wang, F. Jia, Q. Xu, Z. Shu, J. Deng, A. Li, M. Yu, Z. Yu, CXCR4-guided liposomes regulating hypoxic and immunosuppressive microenvironment for sorafenib-resistant tumor treatment, Bioact. Mater. 17 (2022) 147–161.

[9] S. Wang, H. Zheng, L. Zhou, F. Cheng, Z. Liu, H. Zhang, Q. Zhang, Injectable redox and light responsive MnO(2) hybrid hydrogel for simultaneous melanoma therapy and multidrug-resistant bacteria-infected wound healing, Biomaterials 260 (2020) 120314.

[10] W. Niu, Y. Guo, Y. Xue, M. Wang, M. Chen, D.D. Winston, W. Cheng, B. Lei, Biodegradable multifunctional bioactive Eu-Gd-Si-Ca glass nanoplatform for integrative imaging-targeted tumor therapy-recurrence inhibition-tissue repair, Nano Today 38 (2021) 101137.

[11] N.H. Wang, Z.Y. Zhao, X. Xiao, L. Mo, W. Yao, H.K. Yang, J.X. Wang, X.H. Wei, Y. Y. Yuan, R.M. Yang, X.Q. Jiang, ROS-responsive self-activatable photosensitizing agent for photodynamic-immunotherapy of cancer, Acta Biomater. 164 (2023) 511–521.

[12] F. Zhou, B. Feng, H. Yu, D. Wang, T. Wang, Y. Ma, S. Wang, Y. Li, Tumor microenvironment-activatable prodrug vesicles for nanoenabled cancer chemoimmunotherapy combining immunogenic cell death induction and CD47 blockade, Adv. Mater. 31 (14) (2019) e1805888.

[13] M.Y. Wang, M.Y. He, M.Y. Zhang, S.J. Xue, T. Xu, Y.N. Zhao, D.Z. Li, F. Zhi, D. W. Ding, Controllable hypoxia-activated chemotherapy as a dual enhancer for synergistic cancer photodynamic immunotherapy, Biomaterials 301 (2023) 122257.

[14] X. Hu, H. Zhang, Y. Wang, B.-C. Shiu, J.-H. Lin, S. Zhang, C.-W. Lou, T.-T. Li, Synergistic antibacterial strategy based on photodynamic therapy: progress and perspectives, Chem. Eng. J. 450 (2022) 138129.

[15] Z. Zhu, L. Wang, Y. Peng, X. Chu, L. Zhou, Y. Jin, H. Guo, Q. Gao, J. Yang, X. Wang, Z. Long, Y. Ge, S. Lu, B. Wang, Continuous self-oxygenated double-layered hydrogel under natural light for real-time infection monitoring, enhanced

photodynamic therapy, and hypoxia relief in refractory diabetic wounds healing, Adv. Funct. Mater. 32 (32) (2022) 2201875.
[16] M.Y. Wu, L. Chen, Q. Chen, R. Hu, X. Xu, Y. Wang, J. Li, S. Feng, C. Dong, X. L. Zhang, Z. Li, L. Wang, S. Chen, M. Gu, Engineered phage with aggregation-induced emission photosensitizer in cocktail therapy against sepsis, Adv. Mater. 35 (6) (2023) e2208578.
[17] M. Li, R.F. Thorne, R. Shi, X.D. Zhang, J. Li, J. Li, Q. Zhang, M. Wu, L. Liu, DDIT3 directs a dual mechanism to balance glycolysis and oxidative phosphorylation during glutamine deprivation, Adv. Sci. 8 (11) (2021) e2003732.
[18] J.M. Mates, J.A. Campos-Sandoval, J.L. Santos-Jimenez, J. Marquez, Dysregulation of glutaminase and glutamine synthetase in cancer, Cancer Lett. 467 (2019) 29–39.
[19] H.C. Yoo, S.J. Park, M. Nam, J. Kang, K. Kim, J.H. Yeo, J.K. Kim, Y. Heo, H.S. Lee, M.Y. Lee, C.W. Lee, J.S. Kang, Y.H. Kim, J. Lee, J. Choi, G.S. Hwang, S. Bang, J. M. Han, A variant of SLC1A5 is a mitochondrial glutamine transporter for metabolic reprogramming in cancercells, Cell Metabol. 31 (2) (2020) 267–283.
[20] J. Jin, J.K. Byun, Y.K. Choi, K.G. Park, Targeting glutamine metabolism as a therapeutic strategy for cancer, Exp. Mol. Med. 55 (4) (2023) 706–715.
[21] R.D. Leone, J.D. Powell, Metabolism of immune cells in cancer, Nat. Rev. Cancer 20 (9) (2020) 516–531.
[22] S.D. Jeong, B.K. Jung, H.M. Ahn, D. Lee, J. Ha, I. Noh, C.O. Yun, Y.C. Kim, Immunogenic cell death inducing fluorinated mitochondria-disrupting helical polypeptide synergizes with PD-L1 immune checkpoint blockade, Adv. Sci. 8 (7) (2021) 2001308.
[23] L. Xie, G. Wang, W. Sang, J. Li, Z. Zhang, W. Li, J. Yan, Q. Zhao, Y. Dai, Phenolic immunogenic cell death nanoinducer for sensitizing tumor to PD-1 checkpoint blockade immunotherapy, Biomaterials 269 (2021) 120638.
[24] F. Zhou, J. Gao, Y. Tang, Z. Zou, S. Jiao, Z. Zhou, H. Xu, Z.P. Xu, H. Yu, Z. Xu, Engineering chameleon prodrug nanovesicles to increase antigen presentation and inhibit PD-L1 expression for circumventing immune resistance of cancer, Adv. Mater. 33 (43) (2021) e2102668.
[25] T. Wang, D. Wang, H. Yu, B. Feng, F. Zhou, H. Zhang, L. Zhou, S. Jiao, Y. Li, A cancer vaccine-mediated postoperative immunotherapy for recurrent and metastatic tumors, Nat. Commun. 9 (1) (2018) 1532.
[26] E. Preis, J. Schulze, B. Gutberlet, S.R. Pinnapireddy, J. Jedelska, U. Bakowsky, The chorioallantoic membrane as a bio-barrier model for the evaluation of nanoscale drug delivery systems for tumour therapy, Adv. Drug Deliv. Rev. 174 (2021) 317–336.
[27] S. Talebian, J. Foroughi, S.J. Wade, K.L. Vine, A. Dolatshahi-Pirouz, M. Mehrali, J. Conde, G.G. Wallace, Biopolymers for antitumor implantable drug delivery systems: recent advances and future outlook, Adv. Mater. 30 (31) (2018) e1706665.
[28] S.Y. Qin, A.Q. Zhang, S.X. Cheng, L. Rong, X.Z. Zhang, Drug self-delivery systems for cancer therapy, Biomaterials 112 (2017) 234–247.
[29] G. Yuan, Y. Zhang, S. Shao, Z. Zhou, J. Tang, J. Xiang, Y. Shen, Tumor permeable self-delivery nanodrug targeting mitochondria for enhanced chemotherapy, J. Contr. Release 361 (2023) 792–802.
[30] Z. Zhang, C. He, X. Chen, Designing hydrogels for immunomodulation in cancer therapy and regenerative medicine, Adv. Mater. (2023) 2308894.
[31] J. He, Y. Sun, Q. Gao, C. He, K. Yao, T. Wang, M. Xie, K. Yu, J. Nie, Y. Chen, Y. He, Gelatin methacryloyl hydrogel, from standardization, performance, to biomedical application, Adv. Healthcare Mater. 12 (23) (2023) e2300395.
[32] X. Yuan, Z. Zhu, P. Xia, Z. Wang, X. Zhao, X. Jiang, T. Wang, Q. Gao, J. Xu, D. Shan, B. Guo, Q. Yao, Y. He, Tough gelatin hydrogel for tissue engineering, Adv. Sci. 10 (24) (2023) e2301665.
[33] F. Wang, Q. Wu, C. Zhang, L. Kong, R. Zuo, K. Feng, G. Jia, M. Hou, J. Zou, Y. Chai, J. Xu, X. Chen, Q. Kang, Ultrasmall MnOx nanodots catalyze glucose for reactive oxygen species-dependent sequential anti-infection and regeneration therapy, Small Struct (2023) 2300198.
[34] B. Lv, L. Lu, L. Hu, P. Cheng, Y. Hu, X. Xie, G. Dai, B. Mi, X. Liu, G. Liu, Recent advances in GelMA hydrogel transplantation for musculoskeletal disorders and related disease treatment, Theranostics 13 (6) (2023) 2015–2039.
[35] X. Huang, L. Tang, L. Xu, Y. Zhang, G. Li, W. Peng, X. Guo, L. Zhou, C. Liu, X. C. Shen, A NIR-II light-modulated injectable self-healing hydrogel for synergistic photothermal/chemodynamic/chemo-therapy of melanoma and wound healing promotion, J. Mater. Chem. B 10 (38) (2022) 7717–7731.
[36] W. Zhu, Z. Zhou, Y. Huang, H. Liu, N. He, X. Zhu, X. Han, D. Zhou, X. Duan, X. Chen, Y. He, X. Meng, S. Zhu, A versatile 3D-printable hydrogel for antichondrosarcoma, antibacterial, and tissue repair, J. Mater. Sci. Technol. 136 (2023) 200–211.
[37] L.P. Zhao, R.R. Zheng, R.J. Kong, C.Y. Huang, X.N. Rao, N. Yang, A.L. Chen, X. Y. Yu, H. Cheng, S.Y. Li, Self-delivery ternary bioregulators for photodynamic amplified immunotherapy by tumor microenvironment reprogramming, ACS Nano 16 (1) (2022) 1182–1197.
[38] T. Zhu, L. Shi, C. Yu, Y. Dong, F. Qiu, L. Shen, Q. Qian, G. Zhou, X. Zhu, Ferroptosis promotes photodynamic therapy: supramolecular photosensitizer-inducer nanodrug for enhanced cancer treatment, Theranostics 9 (11) (2019) 3293–3307.
[39] B. Kong, Y. Chen, R. Liu, X. Liu, C. Liu, Z. Shao, L. Xiong, X. Liu, W. Sun, S. Mi, Fiber reinforced GelMA hydrogel to induce the regeneration of corneal stroma, Nat. Commun. 11 (1) (2020) 1435.
[40] L. Yang, X. He, Z. Zeng, J. Tang, D. Qi, H. Ma, H. Chen, X. Ning, X. Feng, Clickable amino acid tuned self-assembly of a nucleus-selective multi-component nanoplatform for synergistic cancer therapy, Chem. Sci. 12 (24) (2021) 8394–8400.
[41] X. Qin, M. Zhang, X. Hu, Q. Du, Z. Zhao, Y. Jiang, Y. Luan, Nanoengineering of a newly designed chlorin e6 derivative for amplified photodynamic therapy via regulating lactate metabolism, Nanoscale 13 (27) (2021) 11953–11962.
[42] R. Alzeibak, T.A. Mishchenko, N.Y. Shilyagina, I.V. Balalaeva, M.V. Vedunova, D. V. Krysko, Targeting immunogenic cancer cell death by photodynamic therapy: past, present and future, J. Immunother. Cancer 9 (1) (2021) e001926.
[43] H. Deng, Z. Zhou, W. Yang, L.S. Lin, S. Wang, G. Niu, J. Song, X. Chen, Endoplasmic reticulum targeting to amplify immunogenic cell death for cancer immunotherapy, Nano Lett. 20 (3) (2020) 1928–1933.
[44] Z. Gao, S. Jia, H. Ou, Y. Hong, K. Shan, X. Kong, Z. Wang, G. Feng, D. Ding, An activatable near-infrared afterglow theranostic prodrug with self-sustainable magnification effect of immunogenic cell death, Angew. Chem. Int. Ed. 61 (40) (2022) e202209793.
[45] S. Sen, M. Won, M.S. Levine, Y. Noh, A.C. Sedgwick, J.S. Kim, J.L. Sessler, J. F. Arambula, Metal-based anticancer agents as immunogenic cell death inducers: the past, present, and future, Chem. Soc. Rev. 51 (4) (2022) 1212–1233.
[46] J.J. Wang, M.K. Siu, Y.X. Jiang, T.H. Leung, D.W. Chan, H.G. Wang, H.Y. Ngan, K. K. Chan, A combination of glutaminase inhibitor 968 and PD-L1 blockade boosts the immune response against ovarian cancer, Biomolecules 11 (12) (2021) 1749.
[47] F. Zhou, J. Gao, Z. Xu, T. Li, A. Gao, F. Sun, F. Wang, W. Wang, Y. Geng, F. Zhang, Z.P. Xu, H. Yu, Overcoming immune resistance by sequential prodrug nanovesicles for promoting chemoimmunotherapy of cancer, Nano Today 36 (2021) 101025.
[48] N. Roussot, F. Ghiringhelli, C. Rebe, Tumor immunogenic cell death as a mediator of intratumor CD8 T-cell recruitment, Cells 11 (22) (2022) 3672.
[49] A. Showalter, A. Limaye, J.L. Oyer, R. Igarashi, C. Kittipatarin, A.J. Copik, A. R. Khaled, Cytokines in immunogenic cell death: applications for cancer immunotherapy, Cytokine 97 (2017) 123–132.
[50] J. Cai, Y. Hu, Z. Ye, L. Ye, L. Gao, Y. Wang, Q. Sun, S. Tong, J. Yang, Q. Chen, Immunogenic cell death-related risk signature predicts prognosis and characterizes the tumour microenvironment in lower-grade glioma, Front. Immunol. 13 (2022) 1011757.
[51] Y. Wang, C. Yang, X. Liu, J. Zheng, F. Zhang, D. Wang, Y. Xue, X. Li, S. Shen, L. Shao, Y. Yang, L. Liu, J. Ma, Y. Liu, Transcription factor AP-4 (TFAP4)-upstream ORF coding 66 aa inhibits the malignant behaviors of glioma cells by suppressing the TFAP4/long noncoding RNA 00520/microRNA-520f-3p feedback loop, Cancer Sci. 111 (3) (2020) 891–906.
[52] J. Musa, M.M. Aynaud, O. Mirabeau, O. Delattre, T.G. Grunewald, MYBL2 (B-Myb): a central regulator of cell proliferation, cell survival and differentiation involved in tumorigenesis, Cell Death Dis. 8 (6) (2017) 2895.
[53] A. Karagiota, M. Kourti, G. Simos, I. Mylonis, HIF-1alpha-derived cell-penetrating peptides inhibit ERK-dependent activation of HIF-1 and trigger apoptosis of cancer cells under hypoxia, Cell. Mol. Life Sci. 76 (4) (2019) 809–825.
[54] S. Bengatta, C. Arnould, E. Letavernier, M. Monge, H.M. de Preneuf, Z. Werb, P. Ronco, B. Lelongt, MMP9 and SCF protect from apoptosis in acute kidney injury, J. Am. Soc. Nephrol. 20 (4) (2009) 787–797.